LC-PHSM-2003-xxx
DESY
April/May 2003

Update on flavour tagging studies for TESLA using the BRAHMS simulation (DRAFT version, 24/04/03)

C. J. S. Damerell[1], N. de Groot[1,2], D. J. Jackson[1,3], M. Wing[2], S. M. Xella-Hansen[4]

[1] *Rutherford Appleton Laboratory, Didcot, UK*
[2] *Bristol University, UK*
[3] *Oxford University, UK*
[4] *Zurich-Irchel University, CH*

Abstract.

In this note, the current status of flavour-tagging performed using the BRAHMS simulation is summarised. These studies aim at understanding basic flavour-tagging performance with the current standard TESLA detector configuration and the dependency of the tagging performance on the vertex detector design changes. This is an update and revision of work presented previously [1,2], accounting for detector design and software updates. The results discussed are currently obtained using a standard reference process: $e^+e^- \to q\overline{q}$ at a centre-of-mass energy of 91.2 GeV. A brief look at the same process at higher energies is also presented. More studies, performed on more relevant processes for the future linear collider (FLC), using the SIMDET simulation package, can be found elsewhere [3].

SOFTWARE TOOLS

For this work, the BRAHMS simulation [4] package is used.

Unless otherwise stated, events for the process, $e^+e^- \to q\overline{q}$ at a centre-of-mass energy of 91.2 GeV are considered. This process provides a valuable reference point because the improvement in flavour-tagging performance at the FLC with respect to previous experiments (e.g. LEP/SLC) can be quantified. Also, for flavour tagging, the jets produced in such a process are not so different to those found in higher multiplicity in other processes of greater interest at the FLC, such as $e^+e^- \to HZ$ at 500 GeV [3].

Event generators

Events were generated using the PYTHIA 5.7.20 Monte Carlo (MC) simulation[1] interfaced to the detector simulation package BRAHMS. The process $e^+e^- \to \gamma^*, Z^0 \to q\overline{q}$ is generated and hadronisation is simulated in PYTHIA using JETSET 7.4. The events are then propagated through the GEANT 3 description of the TESLA detector [5]. Beam backgrounds in the simulation are not considered as machine R&D is still ongoing. Noise in the detectors is also not considered and ideal pattern recognition and matching is used as the track reconstruction procedure is still under study. Therefore, the results presented here reflect the pure effects of the new vertex detector design on the physics performance.

Vertex detector

The standard vertex configuration studied here is slightly different from that previously considered [2]. The vertex detector is made of CCD pixels 20x20 μm^2 large, and it has 5 layers at radii 1.55, 2.7, 3.8, 4.9 and 6.0 cm from the beamline, with layer thickness $0.055\% X_0$, where X_0 is the radiation length. the first layer is 10 cm long in the Z-direction, i.e. parallel to the beampipe. The outer four layers are 25 cm long. Only a few optical cables are used to readout the signals, thereby minimising the electronics at the ends of the detector. The simulation of the response of tracks when passing through the vertex detector is quite simple; a layer hit is created by smearing the impact point of the track on the layer by the nominal point resolution (fixed to 3.5 μm).

A main focus of this note is changing the above vertex detector design and determining its impact on heavy-quark tagging and hence its impact on the physics potential of the FLC. Configurations where the first layer is removed, each layer thickness is doubled and combinations of the two are considered.

Track reconstruction

Track reconstruction is performed in three steps. Firstly, Track Elements (TE) are reconstructed in each subdetector. Since ideal pattern recognition is being used, all hits from the track are used[2] and are fitted to one segment. Each vertex detector (VTX) and silicon inner tracker (SIT) hit is considered a TE. Then, all combinations of TEs from different subdetectors are considered, to form candidate tracks, TS. Firstly, merging time projection chamber (TPC) and VTX TEs is attempted, then merging with SIT or forward tracker (FTD) is performed. In this study, fake (wrong combinations) tracks are not allowed. Finally all TS candidates are refitted

---

[1] This version of PYTHIA uses a slightly smaller B lifetime than the updated values in PYTHIA 6.2.

[2] Pattern recognition algorithms from the ALEPH and OPAL experiments are used for TPC and VTX TE reconstruction, respectively.

and form the final track bank, TK. No beam spot constraint is used when finding or fitting the tracks.

Track reconstruction performance and track selection

Appendix A contains distributions determined using a sample of 400000 single tracks (muons and pions) generated in BRAHMS with momenta between 0.05 and 50 GeV and covering all polar and azimuthal angles, using the standard detector configuration. The plots are in bins of polar angle of the generated track ($12-17°$, $17-30°$, $30-60°$, $60-90°$); $12°$ is the minimal angle covered by the 5-layer CCD VTX detector. Only primary tracks are considered and not decay products due to interactions with the material of the detector.

From this study (for more details, see appendix A), needed in order to tune the track selection cuts, the following is concluded:

1. muon and pion reconstruction performance is very similar;

2. the tracking performance is very good (almost 100 % efficient, as expected because of the ideal tracking used) over a large range of momentum (down to 0.1 GeV) and polar angle.

This confirms the very good geometrical coverage of the current design for the TESLA detector and the following track selection criteria can then be defined[3]:

- there should be at least one hit in the VTX along with at least twenty hits in the TPC or at least three hits in the FTD. If the number of hits in the TPC and FTD are fewer, then there should be at least three hits in the VTX.

- p_T should be at least 0.1 GeV

- track should have a maximal impact parameter (point of closest approach to the interaction point (IP)) in $r\phi$ and rz of 2 cm

- χ^2/dof of the track fit should be less than 10

Jet reconstruction

The algorithm for jet reconstruction is a cone algorithm, used by the OPAL collaboration, and is described elsewhere [2]. Different jet reconstruction is not considered here but should be assessed in the future.

---

[3] This allows larger coverage than in previous studies [2].

Primary vertex determination

For all tagging applications a primary vertex is determined, using all found tracks and a beam spot constraint, where the beam spot is assumed to be at (0., 0., 0.) and the beam spread is $0.55.10^{-4}$, $0.50.10^{-6}$, $0.40.10^{-1}$ in (x, y, z) cm, with correlation coefficients (4.10^{-4}, 4.10^{-4}, 0.04). After the primary vertex has been determined, the impact parameters and their significances for all tracks are recalculated with respect to the new primary vertex. This primary vertex is then used in all tagging applications.

Tagging

The tagging procedure is the same followed in the original study [2]. Tagging the jet or the hemisphere (highest energy jet in the hemisphere) is done using a neural network tag, trained on $e^+e^- \to q\overline{q}$ events at a centre-of-mass energy of 91.2 GeV with **three classes**: jets with no, with two or with three or more reconstructed secondary vertices, and with **three outputs**: a b tag output, *bnet*, a c tag output, *cnet*, and a c tag output in the case of no light-quark background, *bcnet*. The inputs for the first class (no secondary vertices) are:

- the first and second most significant impact parameters for a track in the jet, in the $r\phi$ and rz projections;
- the momentum of the track and the angle of the track with respect to the jet axis;
- the joint probability tag for the jet, in $r\phi$ and rz (see next Section).

the inputs for the second and third class are:

- the maximal distance significance between vertices found in the jet by ZVTOP, and the maximal distance between the vertices found.
- the mass and momentum of the jet, calculated using tracks associated to vertices found by ZVTOP
- the number of tracks associated to secondary vertices found by ZVTOP
- the chi-square probability of secondary vertices found by ZVTOP
- the joint probability tag for the jet, in $r\phi$ and rz (see next Section).

Impact parameter joint probability tag

The joint probability tag is based on the original routine used by the ALEPH collaboration [6]. This algorithm uses the impact parameter information from all

tracks in a jet to determine the probability that the track is consistent with coming from the primary vertex. All probabilities are combined to form the tag variable.

Example distributions of impact parameter and impact-parameter significance ($d_0/\sigma(d_0)$) are shown in Fig. 1 for two different centre-of-mass energies, $E_{\rm cm}$. Negative values of impact parameter result from finite detector resolution, where positive values indicate the presence of heavy quark decays. This can be particularly seen in the significance for $E_{\rm cm} = 91.2$ GeV, where beauty events populate preferentially positive values and contribute a large fraction of all events in this region. In Fig. 1, it can also be seen that the distributions differ for differing energies.

In order to keep only events with heavy quarks, the excess they produce in the distribution of impact-parameter significance can be found by parametrising those tracks with no decay. This is achieved by parametrising the distribution for negative significance. The negative side of $x = d_0/\sigma(d_0)$ or $x = z_0/\sigma(z_0)$ are fit with the function

$$f(x) = p_1 e^{-\frac{x^2}{2p_2^2}} + p_3 e^{-\frac{x}{p_4}} + p_5 e^{-\frac{x}{p_6}} + p_7 e^{-\frac{x}{p_8}} \tag{1}$$

and the negative side of $x = 3D/\sigma_{3D}$, is fit with a function:

$$f'(x) = xf(x) = p_1 x e^{-\frac{x^2}{2p_2^2}} + p_3 x e^{-\frac{x}{p_4}} + p_5 x e^{-\frac{x}{p_6}} + p_7 x e^{-\frac{x}{p_8}} \tag{2}$$

The fitted functions are shown in Fig. 2 for each impact parameter significance.

The probability, P_i, that a track has a positive impact-parameter significance is then given by:

$$P_i \;=\; \frac{\int_x^{x_c} f(x)dx}{\int_0^{x_c} f(x)dx} \tag{3}$$

where the integration is performed to some cut-off, x_c, which in this case is 200. The joint probability, P_J, for N tracks from the primary vertex is then given by

$$P_J = y \sum_{m=0}^{N-1} \frac{(-\ln y)^m}{m!} \tag{4}$$

where y is the product of all P_i.

The values obtained for P_J are shown in Fig. 3 for the three impact parameter definitions. As expected, the values for b and c jets peak at low values close to 0, whereas light-flavour (uds) jets exhibit a flatter distribution. The non-flatness in the light-flavour jets arises from long-lived particles and shared primary vertices.

Impact parameter significance

For one-prong B and D decays, where a vertex cannot be determined, a 'one-prong' tag has been used to distinguish these events from light-flavour events. This tag is especially important for charm hadrons, a significant fraction of which are one-prong. The tag is made by looking at the maximal impact parameter

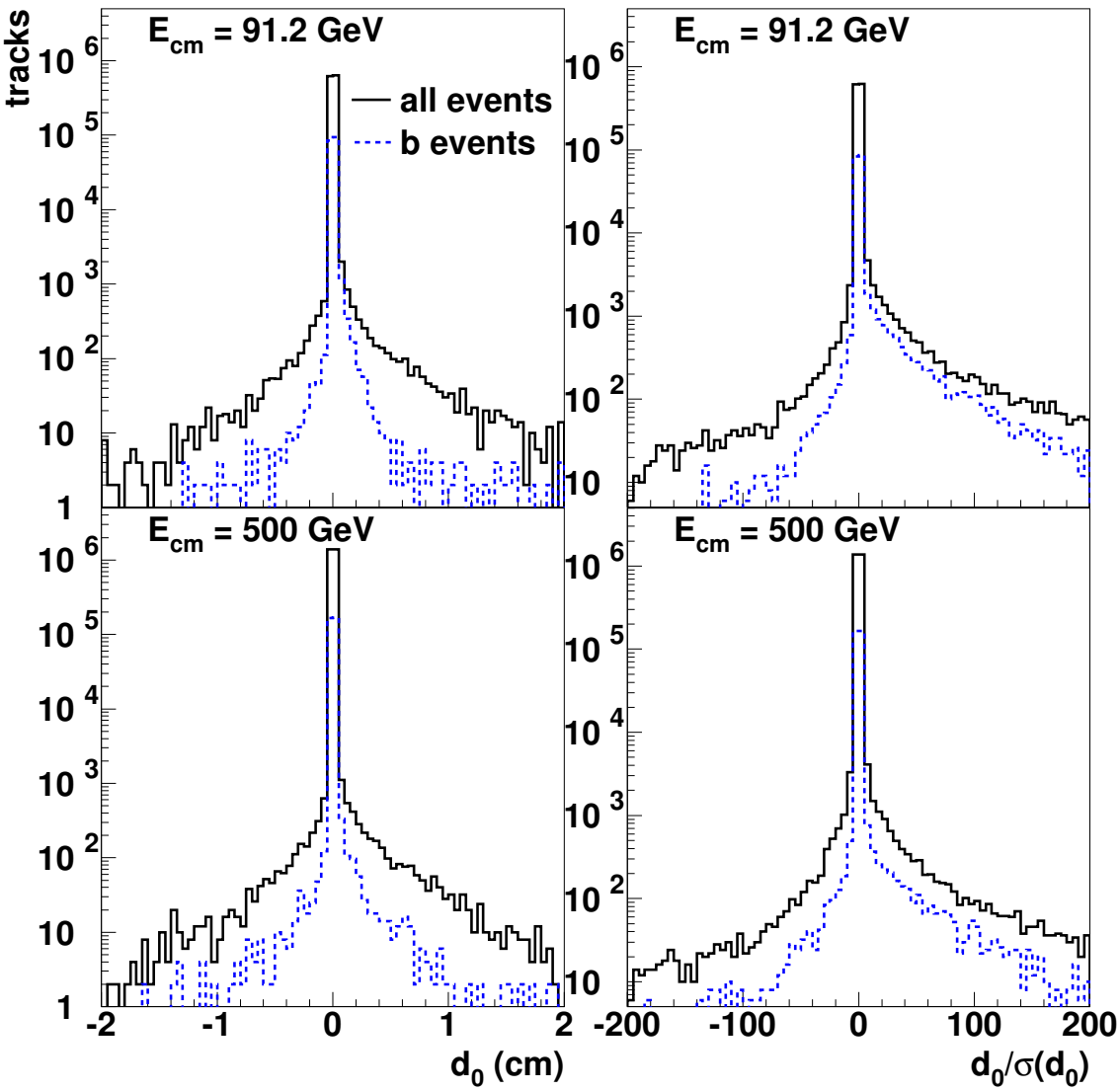

FIGURE 1. Distributions of impact parameter, d_0 and the significance at two different centre-of-mass energies.

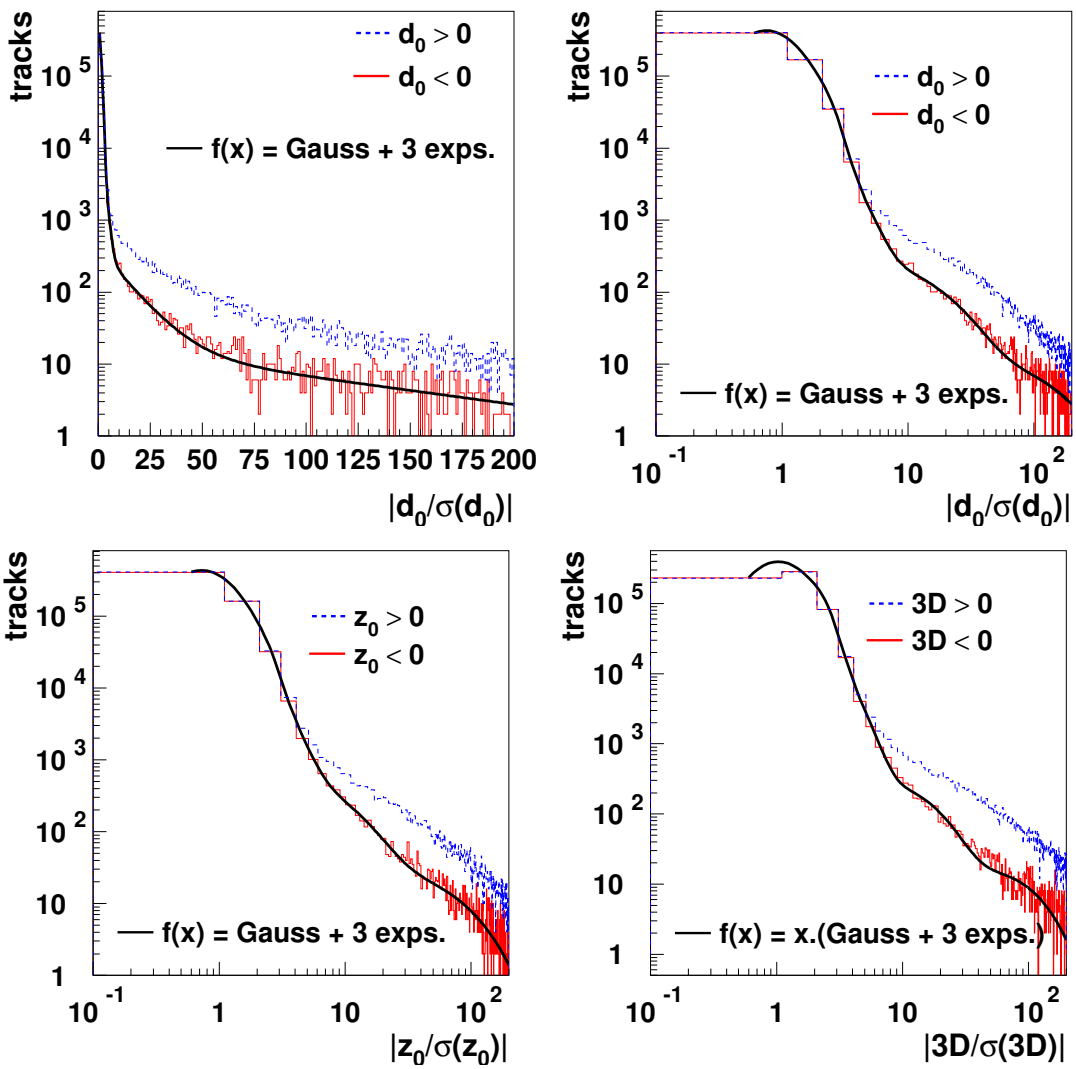

FIGURE 2. Significance distributions for the three impact parameters. For d_0, the distribution is shown on a linear and logarithmic scale. Fits to negative values are shown.

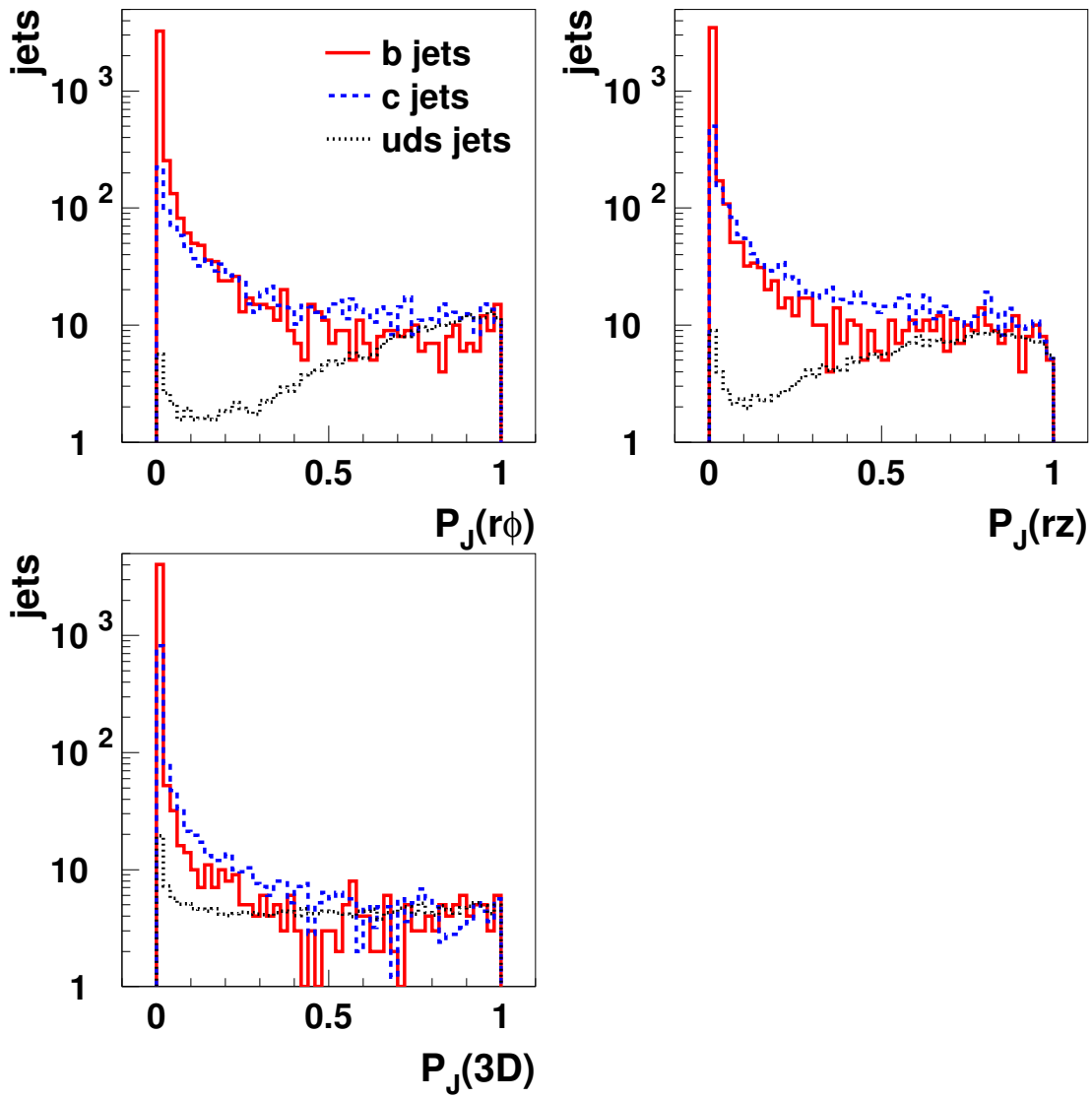

FIGURE 3. Output of the joint probability for the three impact parameters for b, c and light-flavour jets.

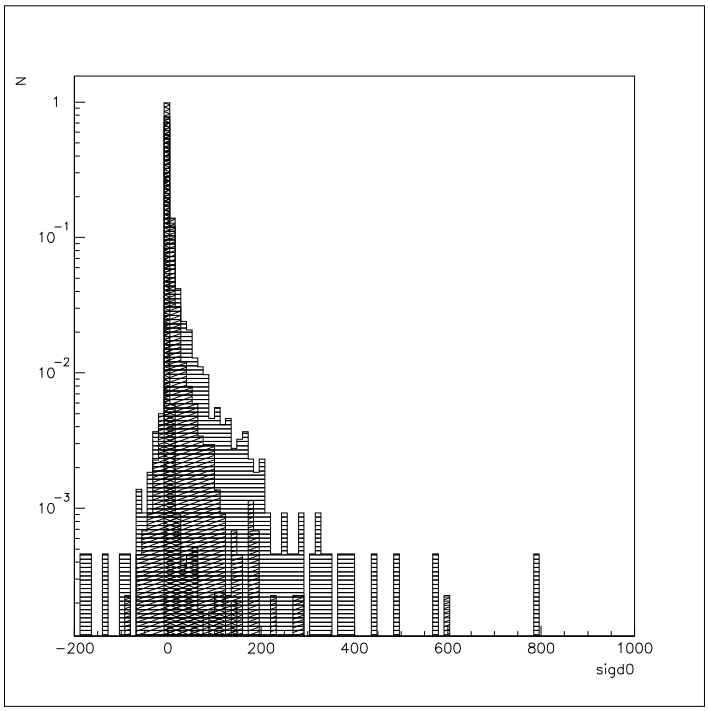

FIGURE 4. Highest $d_0/\sigma(d_0)$ in a jet, for *uds* (inner distribution), *c* and *b* (outer distribution) jets.

significance at the IP of tracks in the jet, in the $r\phi$ and rz planes. Events from b and c quarks are expected to yield an asymmetric distribution whereas light flavours produce a symmetric distribution. This can be seen in Fig. 4.

Jets from *uds* events also have a slight asymmetry. This has been investigated, and is mainly due to tracks coming from decays of light flavour baryons (like Σ) and b and c hadrons from gluon splitting processes. Both of these classes of events have an asymmetric impact parameter distributions.

ZVTOP

`ZVTOP` is the topological vertex finder algorithm used in SLD, and provides very powerful tagging informations like the number of secondary vertices and the reconstructed vertex mass and transverse momentum of the jet. The basic principles of how `ZVTOP` works are explained elsewhere [2,7].

Neural network output

The inputs to the neural network described in the section on Tagging produce the final output for b and c tagging shown in Fig. 5. These are the results of combining all the discriminators described.

Detector configurations

The impact on the physics output due to different detector designs is important for assessing the potential of a future linear collider facility and for optimising the layout of the detector. The nominal design of the vertex detector has been described previously. Two features in its design relevant for physics are the closeness of the innermost layer to the interaction point and the thickness of the active silicon layers. These aspects of the detector have been changed in the simulation and there exist the following options:

1. standard configuration (`turnon(1) = 12`);
2. removing the innermost layer and leaving the others as in the standard configuration, therefore reducing the number of layers to four. The inner radius of the beam-pipe consequently expanded from 1.4 cm to 2.1 cm (`turnon(1) = 22`);
3. doubling the thickness of the active silicon layers from $0.055\%X_0$ to $0.11\%X_0$ (`turnon(1) = 32`);
4. removing the innermost layer and doubling the thickness of the layers, i.e. a combination of (1) and (2) (`turnon(1) = 42`);
5. moving the innermost layer outwards to the nominal position of the second layer, but keeping all five layers. The outer layer was left in the same position as for the nominal design, so the space between the layers was reduced. The inner radius of the beam-pipe was again expanded from 1.4 cm to 2.1 cm (`turnon(1) = 52`).

The above options have been implemented into the BRAHMS package and are controlled by a switch in the `cardsfile`. The switch is `turnon(1)`, where the nominal design of the vertex detector is given by `turnon(1) = 12` and the codes for the other detector configurations are shown above in brackets.

The implementation of the above detector schemes into the fast simulation tool, SIMDET, is more complicated. Here, track parameters are calculated from parametrisations taken from BRAHMS. In particular, the following quantities are parametrised:

- the error on the impact parameter in xy, $\sigma(d_0)$, is parametrised as a function of the track momentum, p, in regions of polar angle, θ as $\sigma(d_0) = a1 + a2/p + a3/p^2 + a4p + a5p^2$, where $a1 - a5$ are constants determined in the fit;

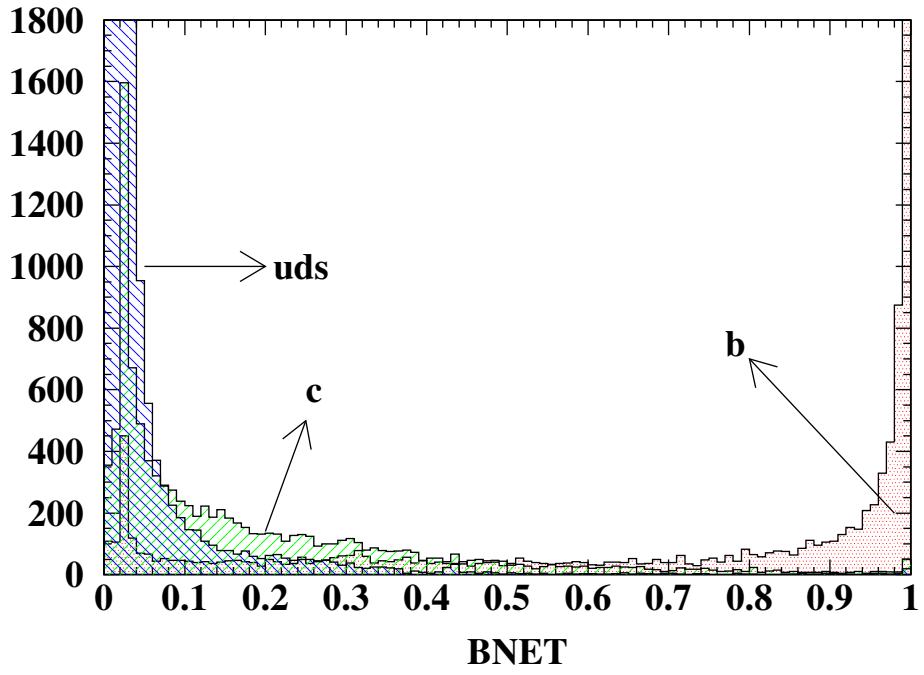

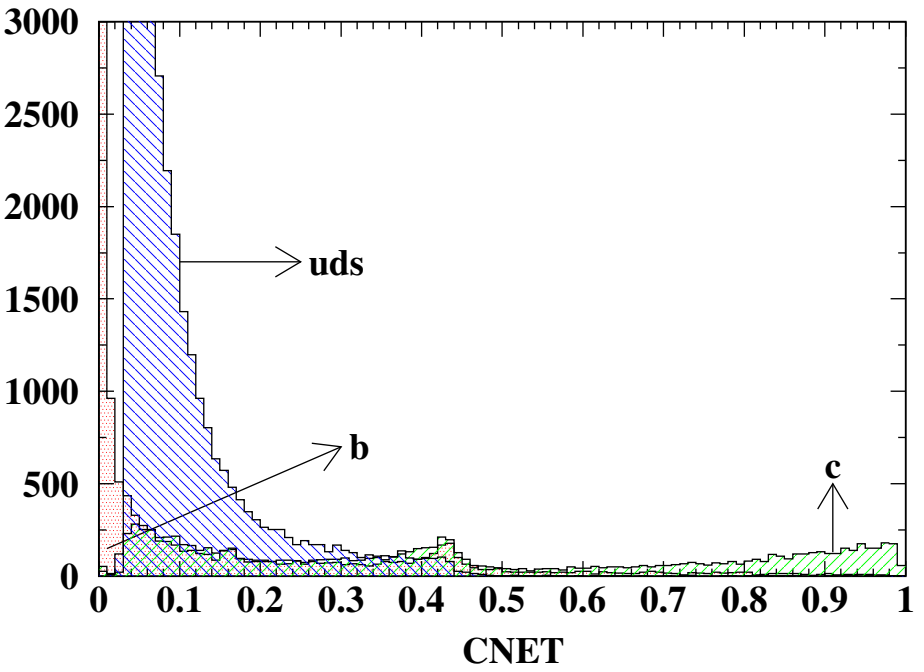

FIGURE 5. Final output of the neural network for tagging b quarks, *bnet* and c quarks, *cnet*. The contribution of the single flavour components is also indicated in the plots

- the error on the impact parameter in rz, $\sigma(z_0)$, is parametrised as a function of the track momentum, p, in regions of polar angle, θ as $\sigma(z_0) = a1 + a2/p + a3/p^2 + a4p + a5p^2$, where $a1 - a5$ are constants determined in the fit;
- the error on the polar angle, $\sigma(\theta)$, is parametrised as a function of θ in regions of p as $\sigma(\theta) = a1 + a2\theta + a3\theta^2 + a4\theta^3 + a5\theta^4$, where $a1 - a5$ are constants determined in the fit;
- the error on the azimuthal angle, $\sigma(\phi)$, is parametrised as a function of θ in regions of p as $\sigma(\phi) = a1 + a2/\theta + a3/\theta^{0.8}$, where $a1 - a3$ are constants determined in the fit;
- the error on the inverse transverse momentum, $\sigma(1/p_T)$, is parametrised as a function of p in regions of θ as $\sigma(1/p_T) = a1 + a2/p + a3/p^2 + a4/p^3 + a5p$ where $a1 - a5$ are constants determined in the fit;

An example of each of the parametrisations is shown in Fig. 6, where different polynomial forms are fitted to data from the BRAHMS simulation. The data used here are single-particle Monte Carlo (MC) tracks generated with PYTHIA. Large samples of pions were generated uniformly in p , θ and ϕ and new parametrisations for each detector configuration found within the range of the vertex detector. To ensure good quality tracks in the vertex detector, cuts as explained previously were used.

In Fig. 6, the two most extreme vertex detector configurations are shown - the standard configuration and removing the innermost layer and doubling the thickness (option 4, above). It can be seen that error on the impact parameters and angles are significantly different between the two designs and the error on the momentum measurement is practically unchanged. The largest difference occurs for the error on the impact parameters at low momentum. The other three detector configurations show similar trends to one of the two shown in Fig. 6, where the most relevant factor is the position of the innermost layer of the vertex detector. Therefore, even though option 5 (above) has five layers, the errors on the track parameters look like those of the four-layer option. This demonstrates the crucial importance of having the innermost layer of the vertex detector as close to the interaction point as possible.

The constants of the fits and parametric forms for the different detector designs are provided in the SIMDET routines `sidcas.f` and `sitrak.f`.

One other parameter in the design is the CCD pixel size. But a detector with larger pixel sizes than 20×20 μ m^2, while maybe preferable for readout speed reasons, gives a worse performance in the reconstruction of tracks in jets (and hence in flavour identification) because of the larger probability for two tracks to deposit charge in the same pixel (or cluster of pixels). The performance gets obviously worse when the c.m.s energy of the process increases. This can be understood when looking at Fig. 7, where the fraction of events having a minimal distance for at least one track pair on layer 1 smaller than some value, is plotted versus that value, for the standard vertex configuration.

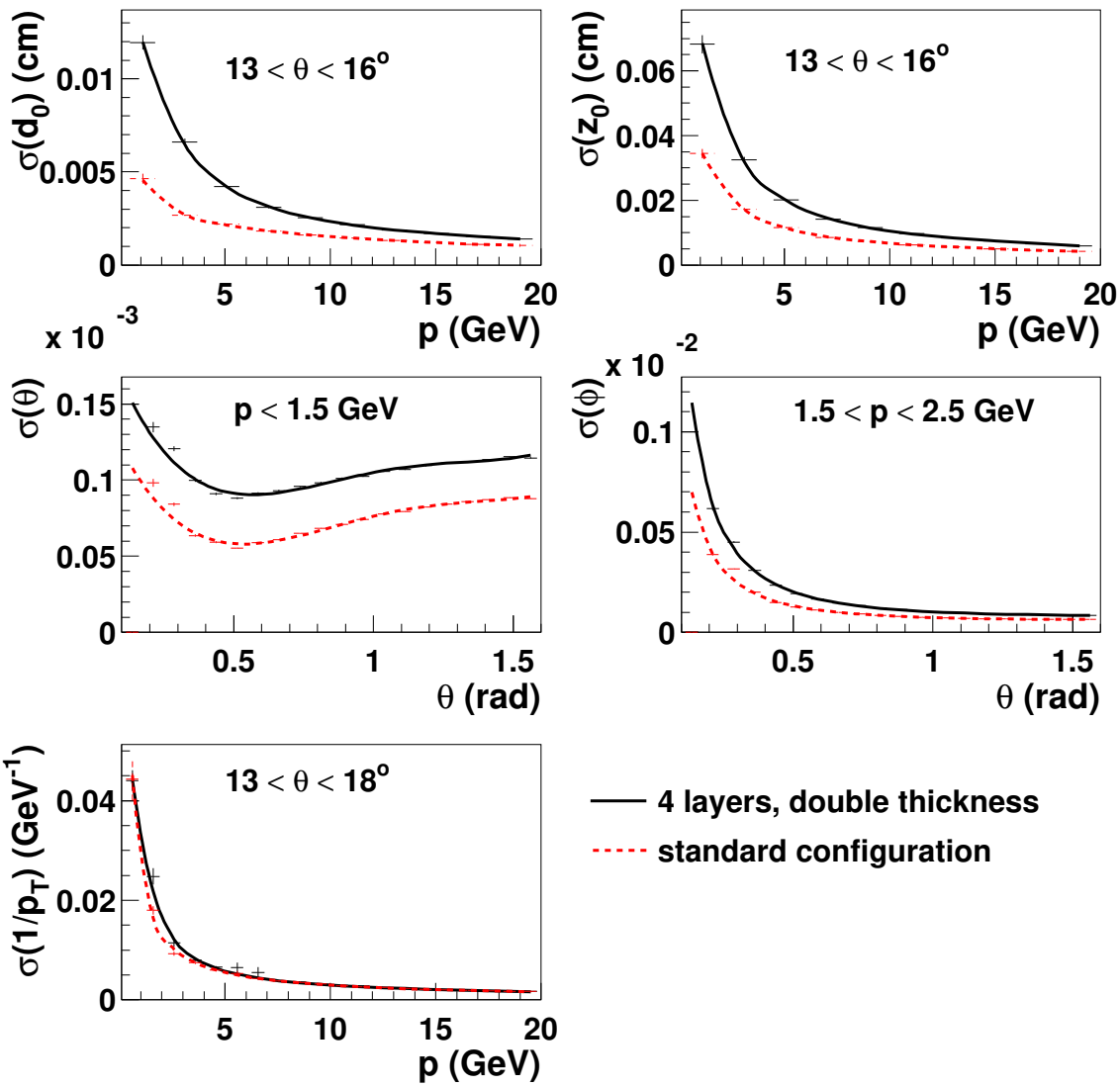

FIGURE 6. Examples of errors on the tracking parameters for pions passing through the vertex detector for two different configurations.

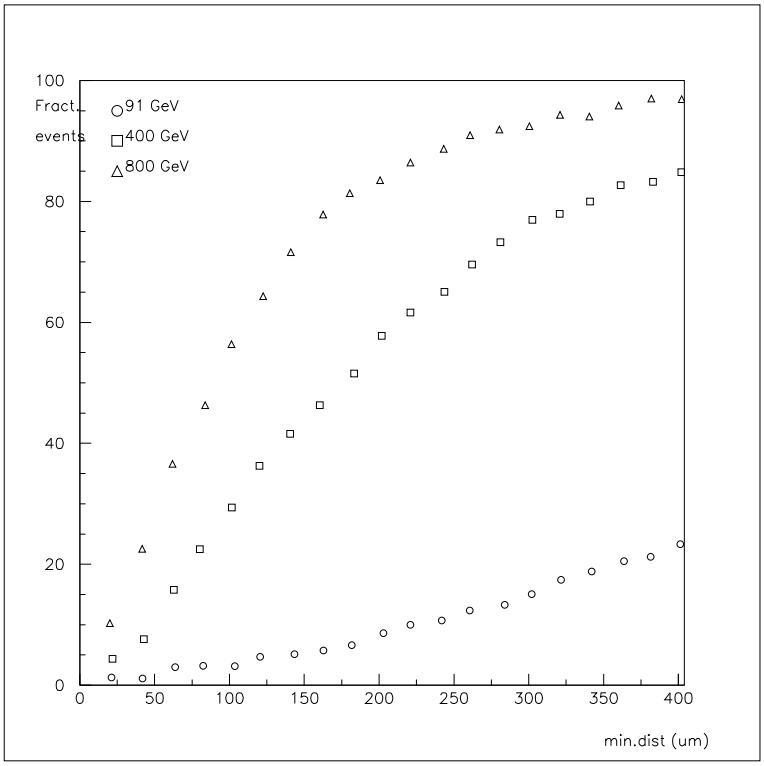

FIGURE 7. Fraction of events having separation in layer 1 smaller than the plotted value in the x-axis, for at least one pair of tracks. Different c.m.s energies results are shown

IMPACT PARAMETER RESOLUTION

The figure of merit for the vertex detector can be expressed by the precision with which the track impact parameter to the IP is measured, separately in the $r\phi$ and rz projections. For a set of cylindrical detectors, this resolution can be expressed as

$$\sigma = \sqrt{a^2 + \left(\frac{b}{p \sin^{3/2}\theta}\right)^2}.$$

The constant a depends on the point resolution and geometrical stability of the detector and b represents the resolution degradation due to multiple scattering, which varies with p and θ. The values of a and b are similar for both projections and, as can be seen in Fig. 8, are 3.1 μm and 4.6 μm, respectively. These values significantly worsen for an alternative detector design as shown in Fig. 8. These numbers can also be compared to the vertex detector at SLD which had values for a and b of 14 μm and 33 μm, respectively.

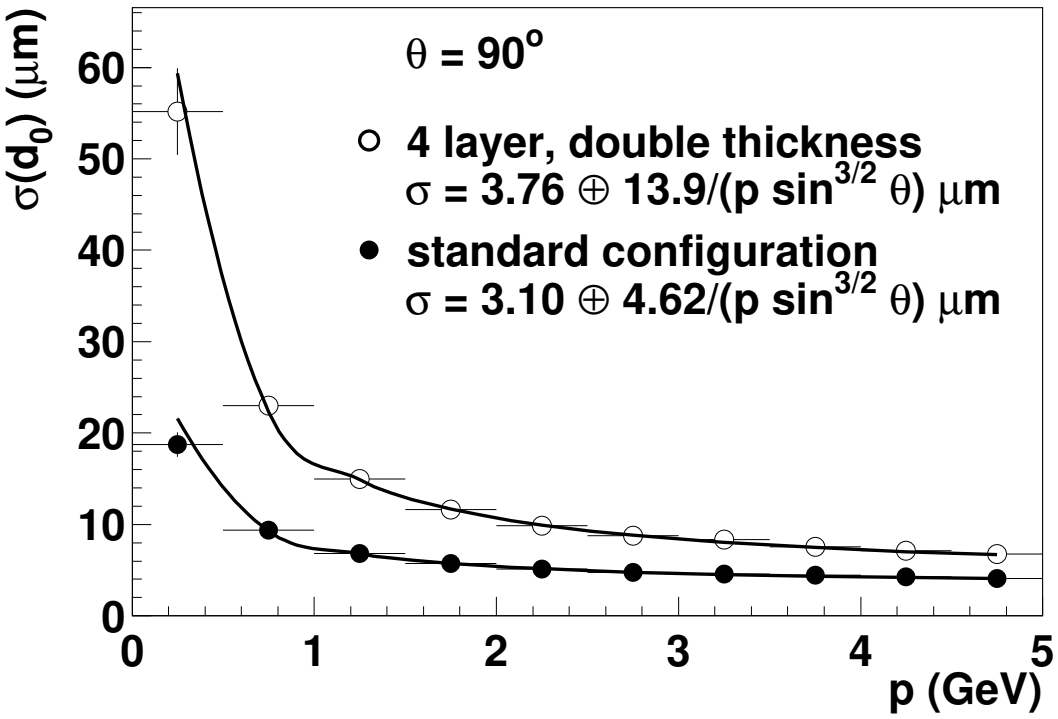

FIGURE 8. Track impact parameter resolution in $r\phi$ versus momentum for tracks at $\theta = 90°$ for two detector configurations.

TAGGING PERFORMANCE

Scanning the values for the neural network output to tag b and c jets, it is possible to trace the purity versus efficiency performance plot shown in Figure 9, for $e^+e^- \to q\overline{q}$ events at 91.2 GeV. The overall performance of the new design for the vertex detector is significantly improved with respect to SLD (see again figure 9. For charm jets, for a similar purity, almost double the efficiency is reached, with respect to SLD. For beauty jets, the purity achievable at efficiencies beyond 60% is much improved. This performance degrades for a detector design with only four layers (`turnon(1) = 42`), particularly in the case of charm tagging.

Figure 10 shows the dependence of the purity of b and c events on the cosine of the jet polar angle, for cuts in the b and c neural network output of 0.48 and 0.43, respectively (corresponding to efficiencies of 80% and 50%, respectively). The reduction in performance at the edges of the angular coverage (which is important for physics) is modest.

The tagging performance shown here, as well as the impact parameter resolution shown in the previous section, are slightly different from that in the TDR [5] due to the different initial track selection used in the two cases. The new selection is optimized for vertex charge performance (see later).

HIGHER ENERGY RESULTS

It is important to study the dependence of the performance of the tagging algorithm on jet energy, since the TeV-scale collider will include events with a wide range of jet energies. Figures 11 and 12 show the variation in quality of the flavour tagging with jet energy, in monojet events. This study has been carried out generating monojets with PYTHIA, and is based on a neural net training used for studies of the $e^+e^- \to q\overline{q}$ events. The figures show the efficiency for tagging each 'unwanted' flavour as function of the efficiency for tagging the 'wanted' flavour. As seen in the figures, the power for rejecting unwanted flavours (for a given efficiency for the wanted flavour) is extremely stable. The performance shown in these figures should not be expected to be exactly the same for 'real' physics processes at the linear collider. The monojets events here simulated are 'unphysical', and used purely to test the performance of the tagging algorithm with energy.

For events $e^+e^- \to q\overline{q}$ at $E_{\rm cm} = 500$ GeV, the purity versus efficiency is shown in Fig. 13. In comparison to lower energies, the c tagging is dramatically improved, both globally and when b quark events are the only background. The b tagging appears to be worse, but arises from the different quark compositions at the two different energies and the increased fraction of gluon splitting events at higher energies. If both of these factors are accounted for, the performance as for $E_{\rm cm} = 91$ GeV is retrieved.

One can also observe a significant degradation of the performance when looking at a design with only four layers and double thickness (`turnon(1) = 42`).

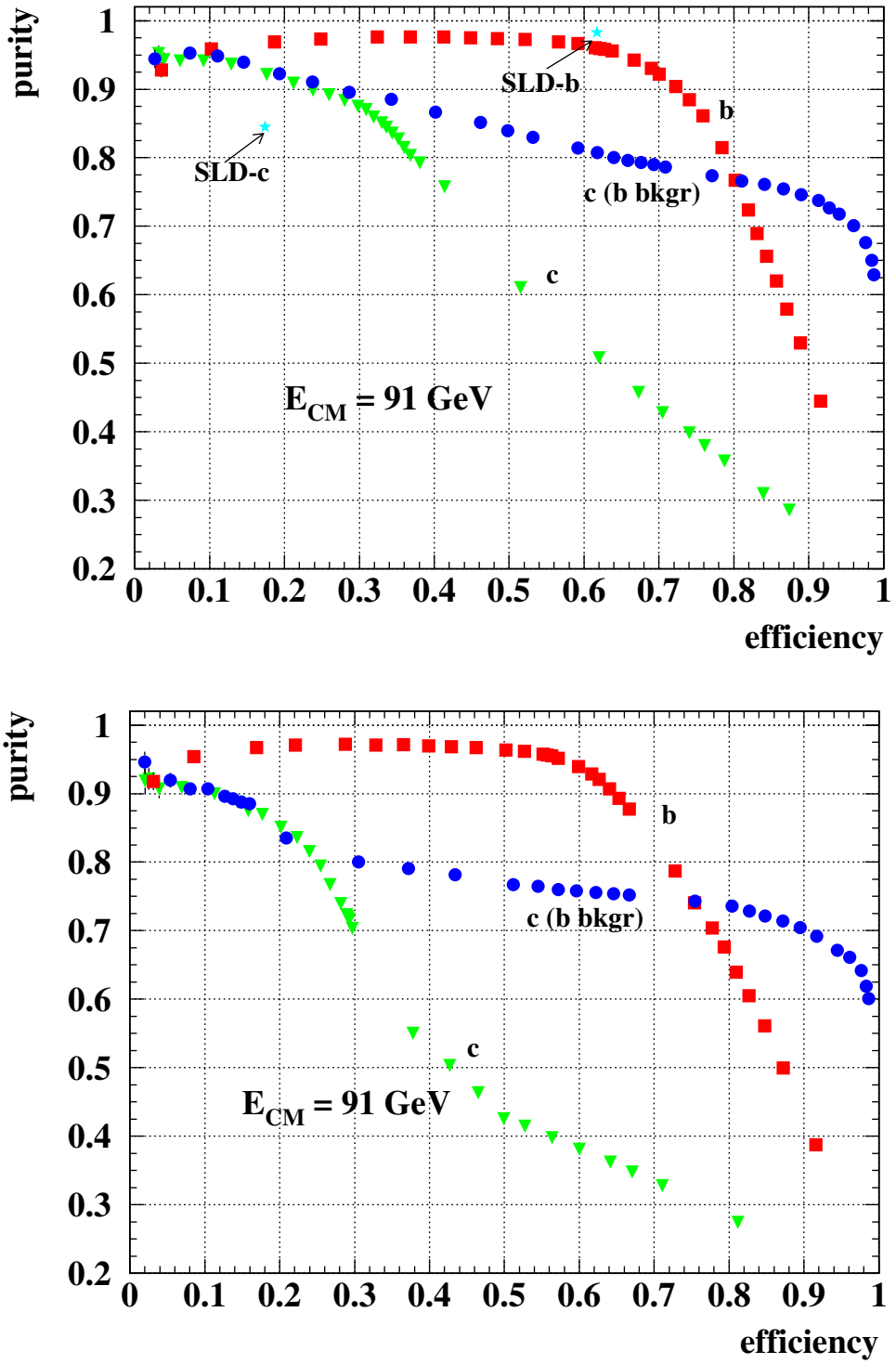

FIGURE 9. Purity versus efficiency for $e^+e^- \to q\overline{q}$ at $E_{\rm cm} = 91.2$ GeV for the standard detector configuration (top) and a vertex detector with four layers and double thickness (bottom). Tagging is done on the hemisphere (highest energy jet).

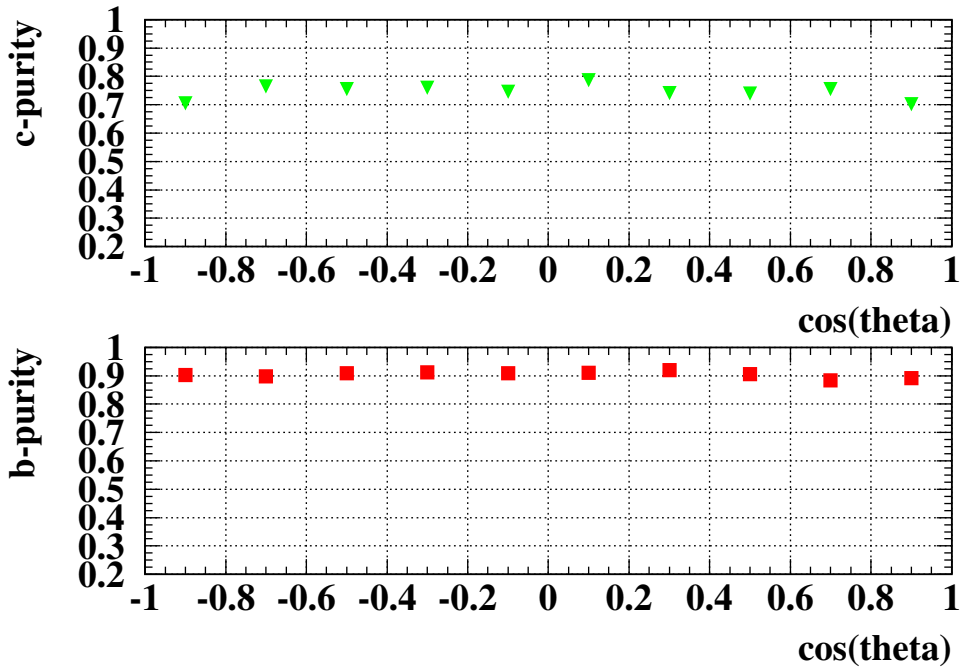

FIGURE 10. Purity versus cosine of the jet angle for beauty (top) and charm (bottom) flavour jets, for $e^+e^- \to q\overline{q}$ at $E_{\rm cm} = 91.2$ GeV.

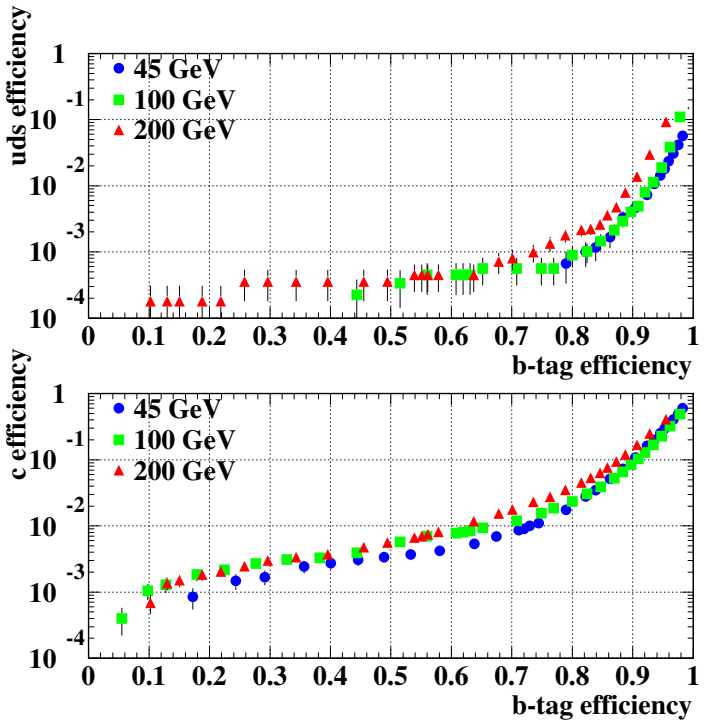

FIGURE 11. Tagging performance for b jets of different energies. Efficiencies for 'unwanted' uds jets and charm jets are shown as function of the b-tag efficiency

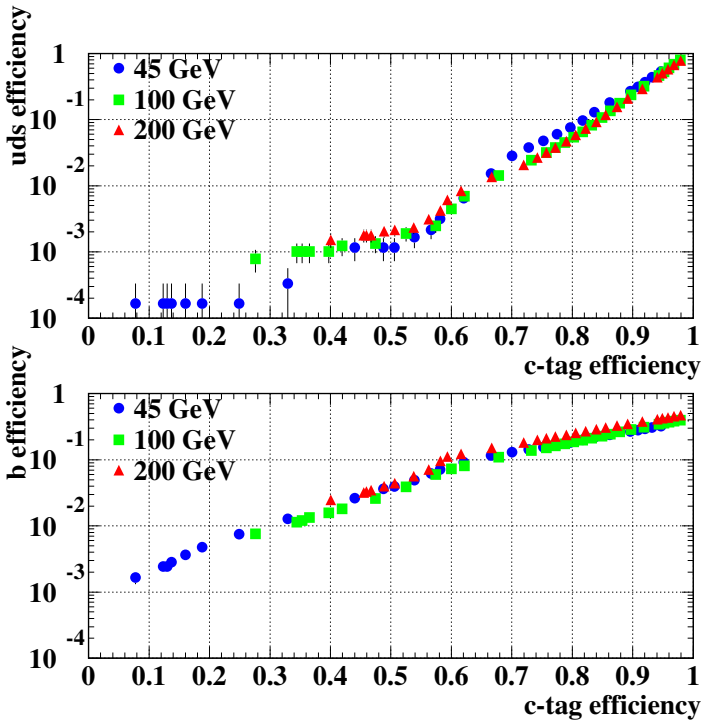

FIGURE 12. Tagging performance for charm jets of different energies. Efficiencies for 'unwanted' *uds* jets and *b* jets are shown as function of the *c*-tag efficiency

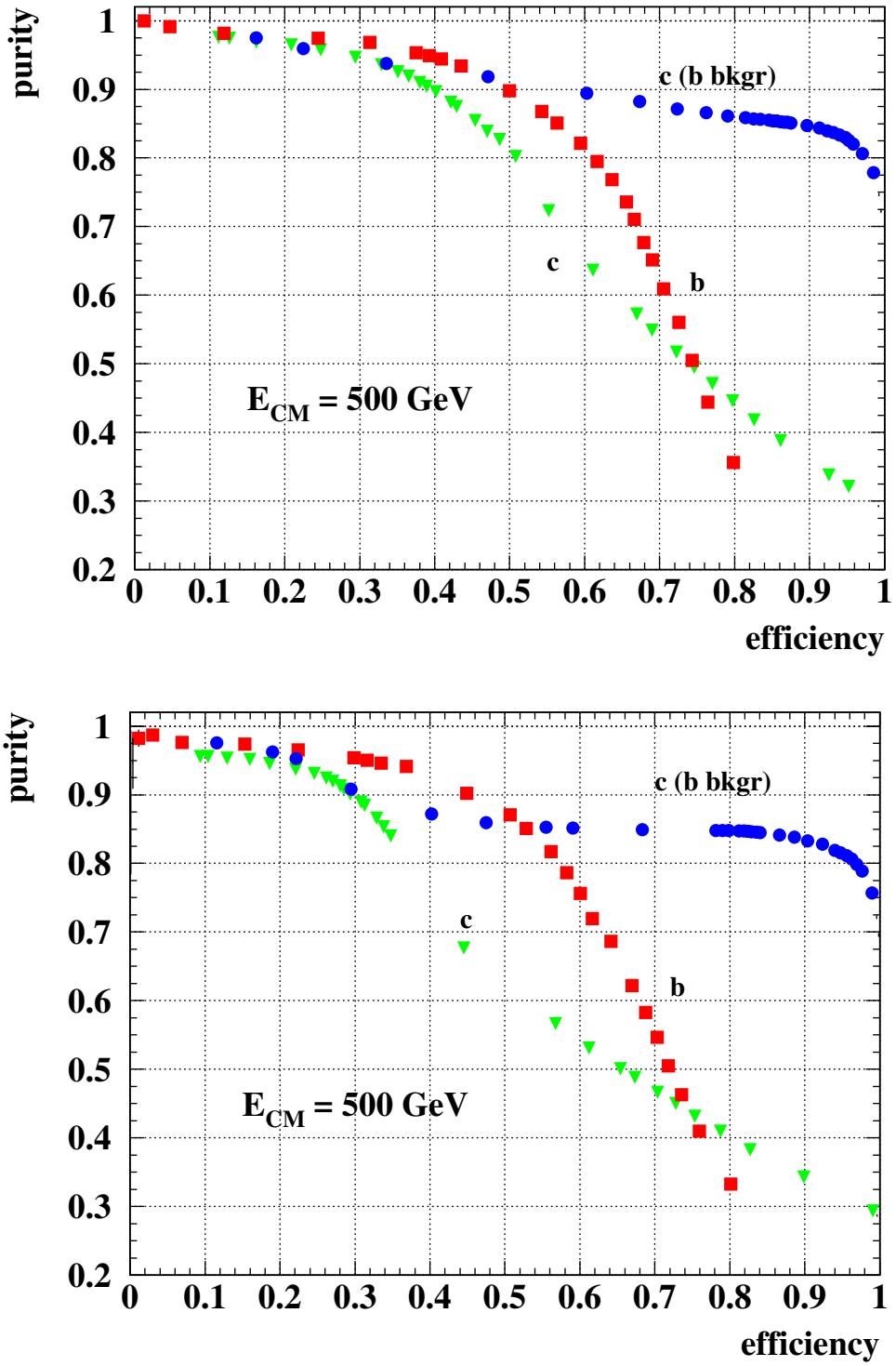

FIGURE 13. Purity versus efficiency for $e^+e^- \to q\overline{q}$ at $E_{\rm cm} = 500$ GeV for the standard detector configuration (top) and a vertex detector with four layers and double thickness (bottom). Tagging is done on the hemisphere (highest energy jet)

QUARK CHARGE IDENTIFICATION

After identifiying the heavy quarks, determining their charge is important for measuring asymmetries or to suppress combinatorical background. We employ two techniques, vertex charge for charged mesons, and dipole for neutral B mesons.

vertex charge

When one or more secondary vertices are found in a jet, we use the one with the longest distance to the IP as a starting point. We loop over all tracks in the event and the tracks that meet the following requirements are attached to the vertex:

- Transverse distance of the point of closest approach (POC)of the track to the line connecting the IP and the secondary vertex of less than 0.1 mm.
- Longitudinal distance of the POC from the IP (L) more than 0.025 mm.
- L divided by the vertex decay length (D) greater than 0.2 (L/D ¿ 0.2)

The charge of all the tracks attached to the vertex is summed and if different from 0 it is used to identify the charge of the quark. We managed to improve the vertex charge performance slightly by feeding the above variables and the angle between the track and the vertex direction into a neural network.

Figure 14 shows the performance of the vertex charge for charged B's. A purity of up to 90% can be achieved for a long range of efficiencies. The vertex charge for B's is very sensitive to the detector configurations, as can be seen from the degrade performance of the 4-layer detector.

Figure 15 shows the performance of the vertex charge for charged D mesons. High purities can be acieved. This is beacuse the D-meson has a low multiplicity and the tracks are usually higher momentum that for the B. For most of the efficiency range the performance of the two configurations is simular. When going to high efficiency, which means including D's with a shorter decay length, a clear difference can be observed.

dipole

For neutral b or c hadrons it is not possible to use vertex charge. In the case of a B^0 we can use the cascade structure of the $b \to c \to s$ decay. Because of the lifetime of the D meson, a b quark can lead to a negatively charged secondary vertex and a positively charged tertiary vertex.

The dipole method leads to a 70% right charge assignment for B^0 mesons, which have a mixing of $\chi = 0.181$. If we include all vertices with reconstructed charge of 0, B_s mesons, b baryons and incorrectly reconstructed charged B's, this drops to 60%. The effect of the dipole can de improved using a cut on decay length, or by using its strength in a likelihood or event weight.

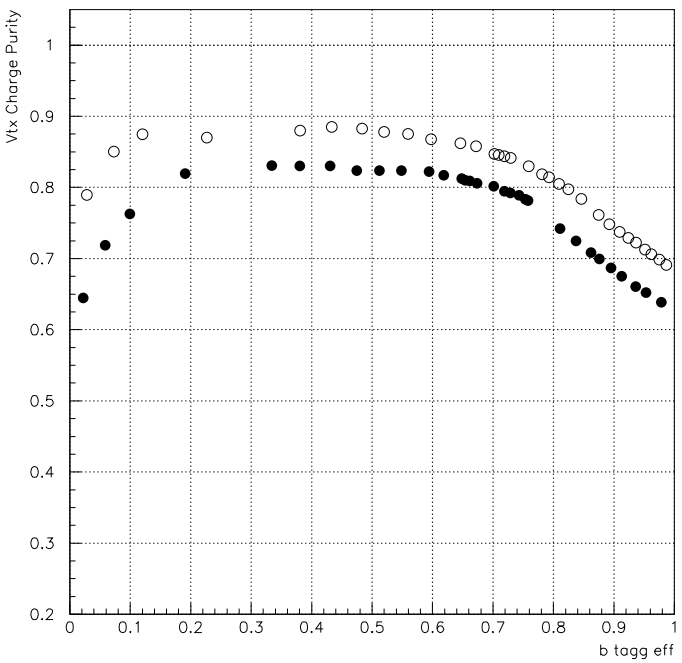

FIGURE 14. Fraction of correctly tagged $B^{\pm}$ standard configuration (open) and the 4 layer double thickness detector (closed) as a function of the fraction of $B^{\pm}$'s with a secondary vertex.

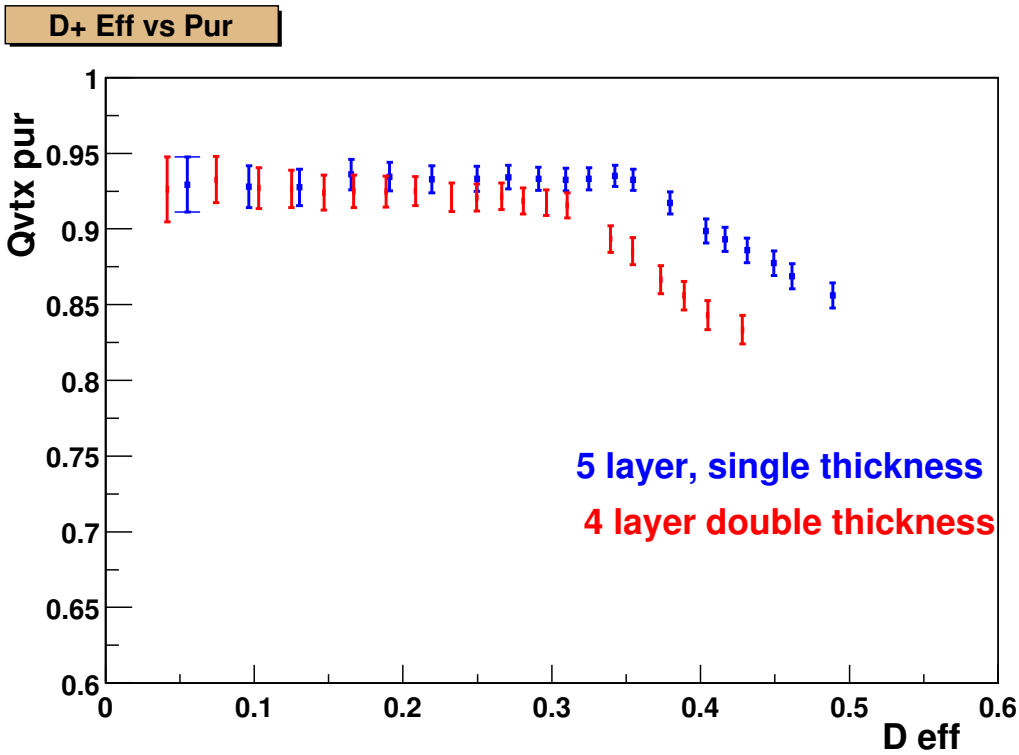

FIGURE 15. Fraction of correctly tagged $D^{\pm}$'s with a reconstructed vertex charge different from 0 for the standard configuration (blue) and the 4 layer double thickness detector (red) as a funtion of the fraction of $D^{\pm}$'s.

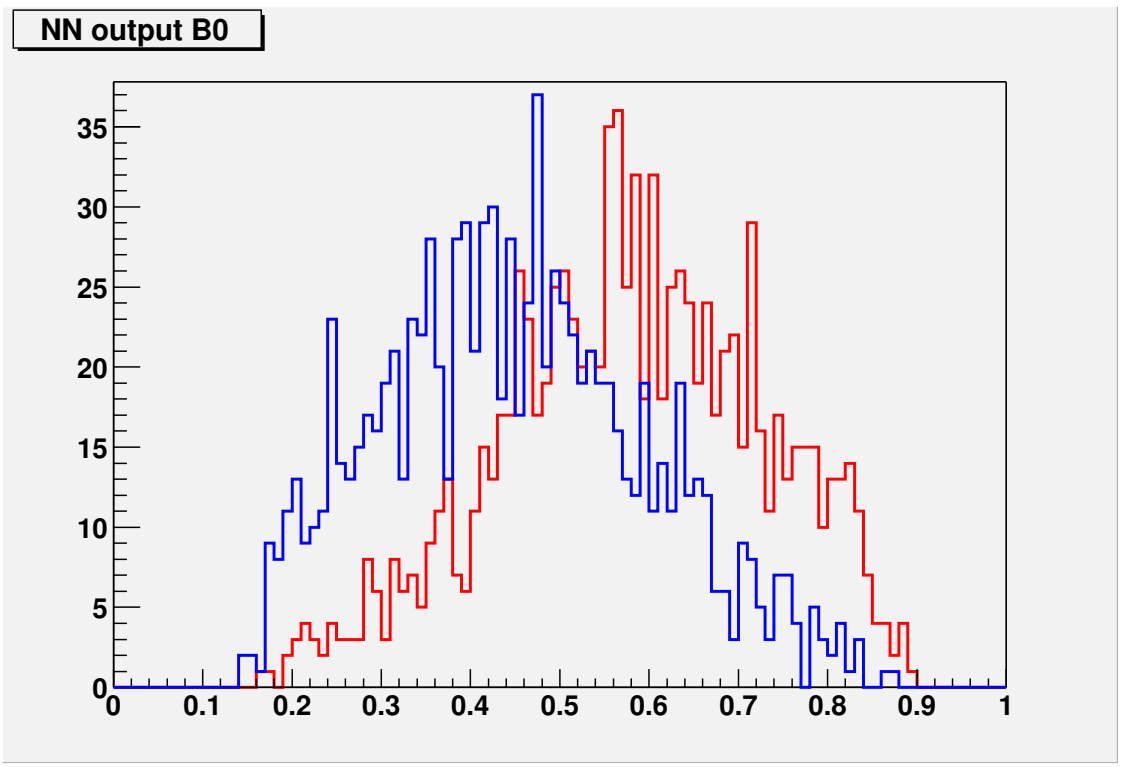

FIGURE 16. Dipole signal for B^0 (red) and $\bar{B}^0$ (blue)

CONCLUSIONS

This note has extended studies of flavour tagging at a FLC. Different energies and designs of the vertex detector have been considered and the performance of the flavour-tagging algorithms assessed. It has been shown that the performance of the algorithms is the same for b quarks and improved for c quarks at higher energies. Changing designs of the vertex detector can lead to significantly poorer measurements of, for example, impact parameters. This leads to a reduced performance in flavour tagging. The impact of this on more interesting physics processes is in progress.

REFERENCES

1. S. Xella-Hansen *et* al., LC-PHSM-2001-024. S. Xella-Hansen (for the LCFI collaboration), "Flavour tagging at the future linear collider", Nucl. Instr. Meth. **A 501** (2003) 106.
2. R. Hawkings, "Vertex detector and flavour tagging studies for the TESLA linear collider", LC-PHSM-2000-021
3. T. Kuhl et al., LC note on SIMDET and flavour tagging.
4. `www-zeuthen.desy.de/linear_collider`
5. `www.tesla.desy.de`
6. ALEPH coll., D. Buskulic et al., Phys. Lett. **B 313** (1993) 535.
7. D. J. Jackson, "A topological vertex reconstruction algorithm for hadronic jets", Nucl. Instr. Meth. **A 388** (1997) 247.

APPENDIX A

A sample of 400000 single tracks (muons and pions) were generated in BRAHMS with momenta between 0.05 and 50 GeV and covering all polar and azimuthal angles.

The following track categories were defined:

name	meaning
GA	% of tracks with nhvtx.ge.1.and.(nhtpc.ge.20.or.nhftd.ge.3)
GB	% of tracks with nhvtx.ge.3.and.nhtpc.lt.20.and.nhftd.lt.3
GC	% of tracks with nhvtx.lt.3.and.nhtpc.lt.20.and.nhftd.lt.3
GD	% of tracks with nhvtx.eq.0.and.(nhtpc.ge.20.or.nhftd.ge.3)

GA, GB, GC and GD are fractions of generated tracks. FA, FB, FC and FD are fractions of reconstructed tracks.

The polar angle regions $12-17^\circ$, $17-30^\circ$, $30-60^\circ$ and $60-90^\circ$ were considered.

Summary

Detector design and material are such that with decreasing momentum GA decreases and GB increases (noticeable effect for p<1 GeV). The sum of GA and GB is always about 1. A very careful understanding of the material description and design is needed to understand if this can be improved.

Track reconstruction is not perfect (as expected from using ideal pattern recognition and ideal merging). This is why tracks initially in class GA do not end up in FA. At low momentum this effect is stronger because most of them are actually spiralling due to the magnetic field. They have many more hits in the TPC, FTD and SIT than usual (i.e. than what a track in full acceptance and with high momentum would have), due to the spiralling trajectory (same radius hit more than once). Because of this (see definition of GA above) t hey end up in GA, but these tracks are very difficult to reconstruct. We most probably have to live with them.

At higher momentum (>2 GeV) and at high angles (30-90 degrees) there is a not expected effect of GA tracks migrating to classes FB, FC and FD, due to

(a) tracks having TPC, SIT and VTX 'TE' segments reconstructed, but having only the VTX and some of the SIT 'TE's used to make the final track (TPC piece is thrown away at merging stage, after 'TS' is made)

(b) tracks having TPC, SIT and VTX 'TE' segments reconstructed, and generating two final tracks, one with TPC 'TE', and one with VTX and some of the SIT TEs (this happens at 'TS' formation stage).

(c) there is a difference between TPC hits generated and used, and this happens at the 'TE' making stage.

(a) and (b) are called *s*plit tracks. This is clearly an effect of the reconstruction procedure, which could not be excluded completely from this analysis (in order to study only pure effect designs). Some material fine tuning, and revision of track reconstruction procedure might improve points (a), (b) and (c). (b) and (c) are smaller effects than (a). The (a)+(b) subclass of tracks is delicate, because the momentum is not always well reconstructed, and this also degrades the resolution on the track parameters (i.e. create bands at high values in the impact parameter error versus momentum plots at high angles). These tracks represent about 1% of the total amount of tracks generated over the whole momentum-angle range (similar value for pions and muons). This split-track phenomenon also affects $b\overline{b}$ events at 91.2 GeV. About 11% of the jets are affected by it: 5% do not contain one or more b daughters because of this, and 6% contain one or more b daughters affected by this.

In reality a good fraction of these tracks, even if they loose the TPC 'TE', thanks to even just 1 hit in SIT manage to get a decent momentum estimation and hence a good impact parameter estimation (and realistic error). This fraction explains the 6% of jets containing b daughters affected by the split-track phenomenon.

Two additional comments. First, the percentages above do not include the effect (mainly at low momentum) of GA decreasing with momentum decreasing (and GB increasing accordingly). This is connected to the material and design of the current detector, and not to the track reconstruction. Secondly, in some bins of momentum the sum of FA and FB is greater than 1 because of the phenomenon where one good track in GA is split during reconstruction into a TPC/FTD and VTX TK, hence giving a track in FB and a track in FD category.

In each of the following plots, the top plot shows the fractions G_i and F_i defined above, and the bottom plot shows the impact parameter error in $r\phi$ (μm) versus momentum for the different F_i classes. The results are for the standard vertex detector configuration for figures 17- 24, and for the configuration with four layers and doubler thickness for figures 25- 32.

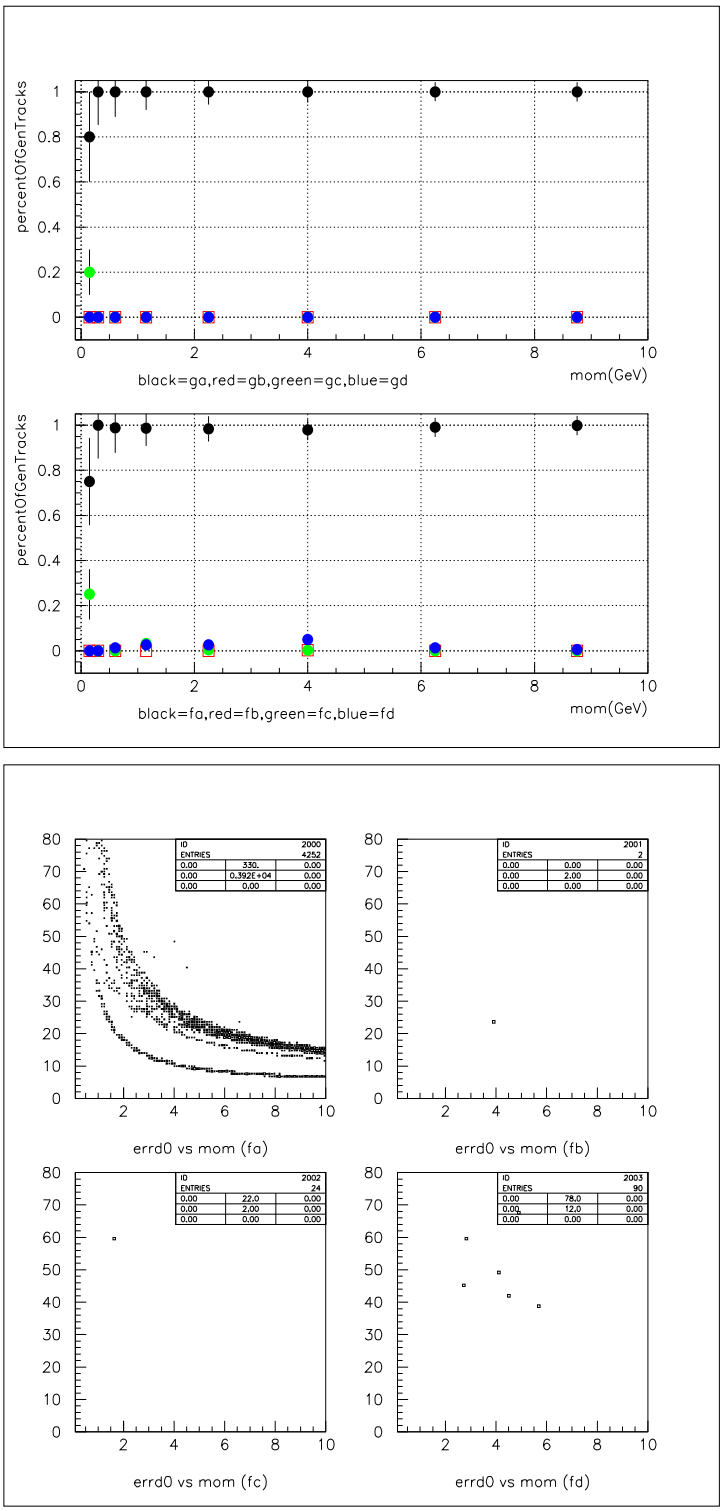

FIGURE 17. G_i and F_i (top) and impact parameter error in $r\phi$ (in μm) versus momentum (in GeV) for the different F_i (bottom), for polar angle range $12 - 17°$ muon tracks.

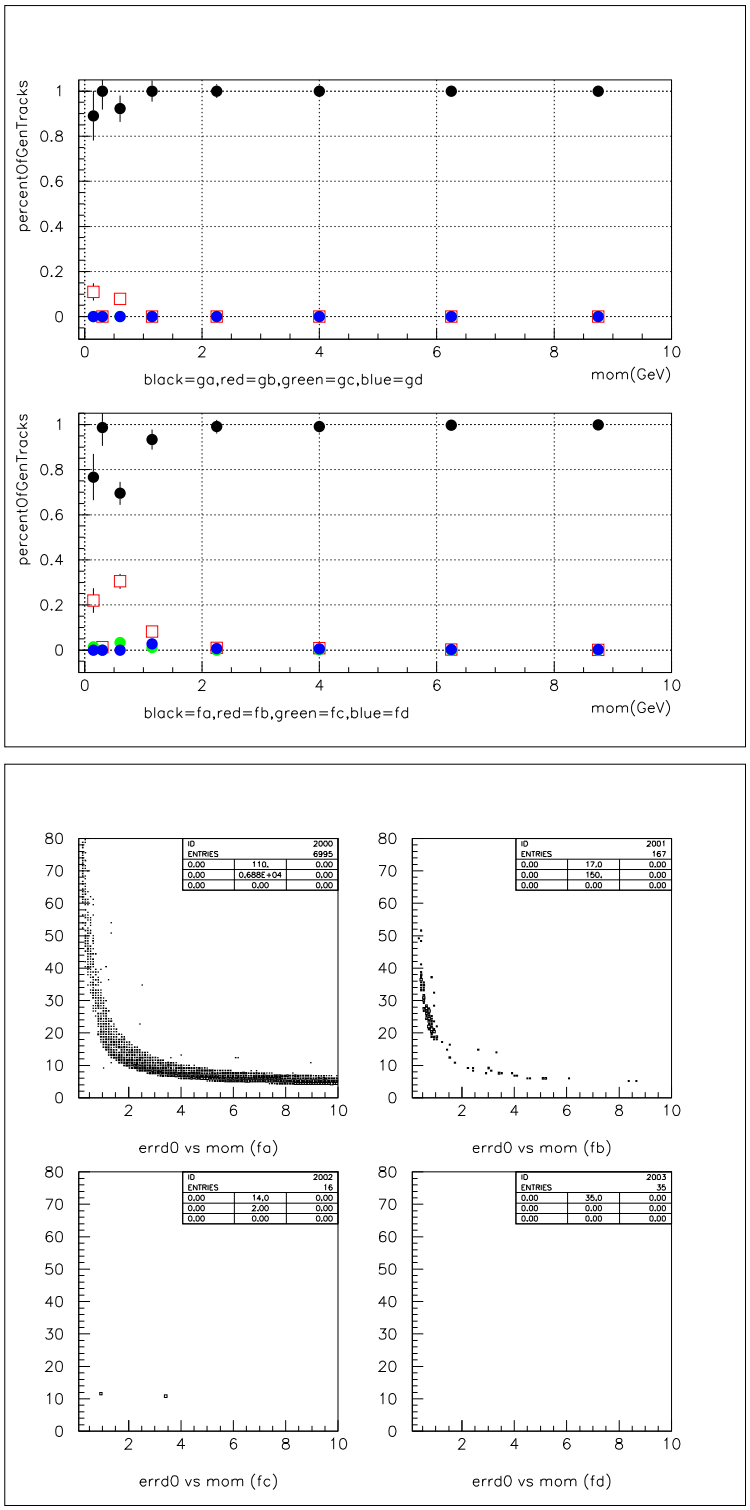

FIGURE 18. G_i and F_i (top) and impact parameter error in $r\phi$ (in μm) versus momentum (in GeV) for the different F_i (bottom), for polar angle range $17 - 30^\circ$ muon tracks.

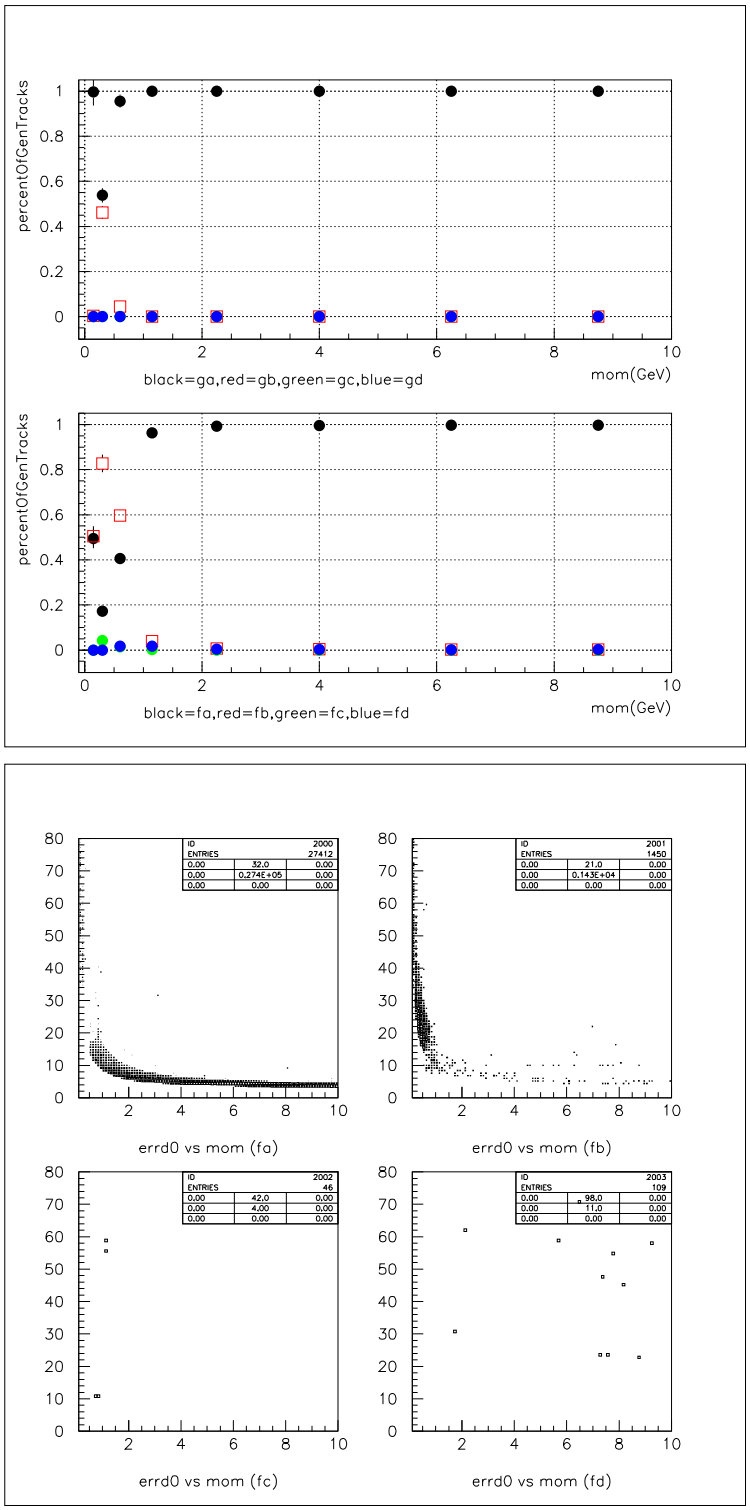

FIGURE 19. G_i and F_i (top) and impact parameter error in $r\phi$ (in μm) versus momentum (in GeV) for the different F_i (bottom), for polar angle range $30 - 60^\circ$ muon tracks.

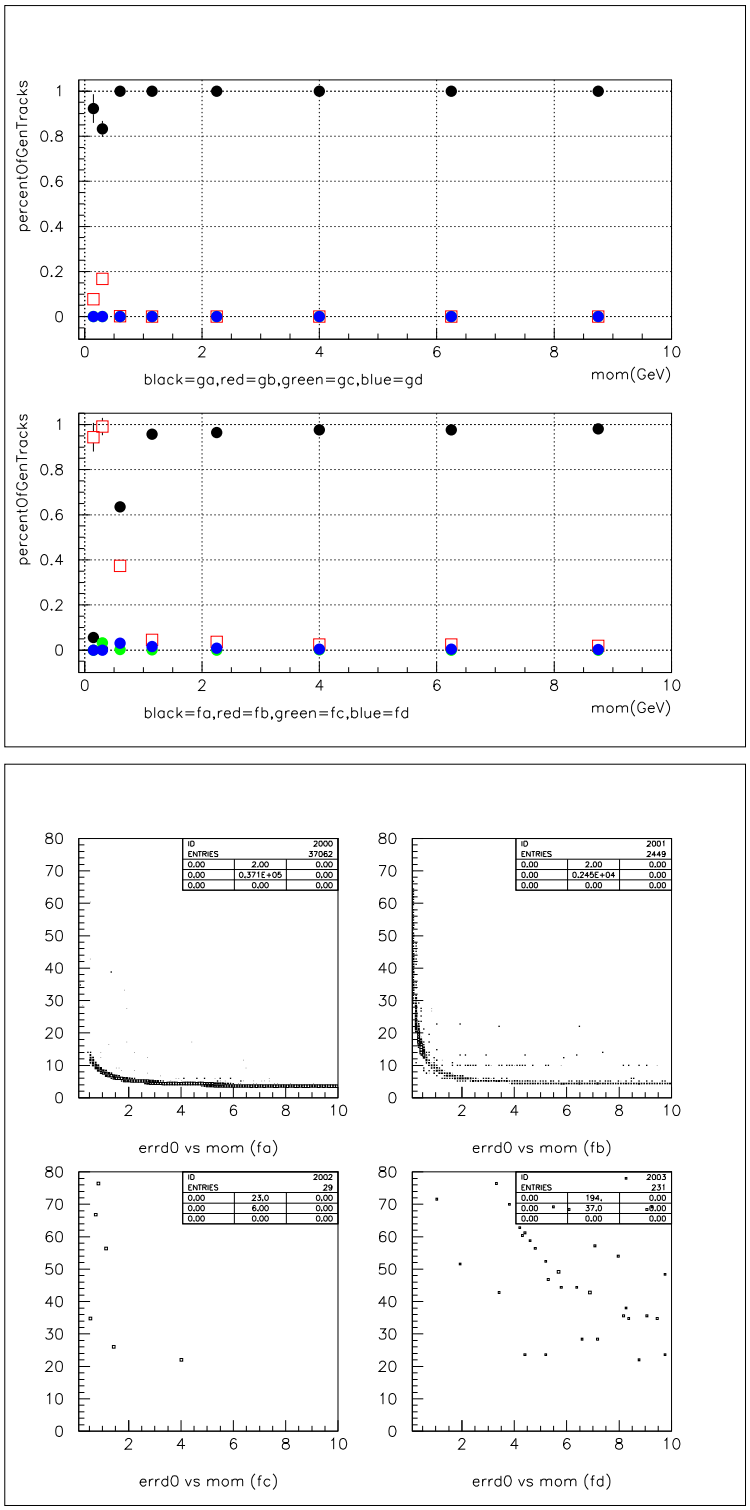

FIGURE 20. G_i and F_i (top) and impact parameter error in $r\phi$ (in μm) versus momentum (in GeV) for the different F_i (bottom), for polar angle range $60 - 90°$ muon tracks.

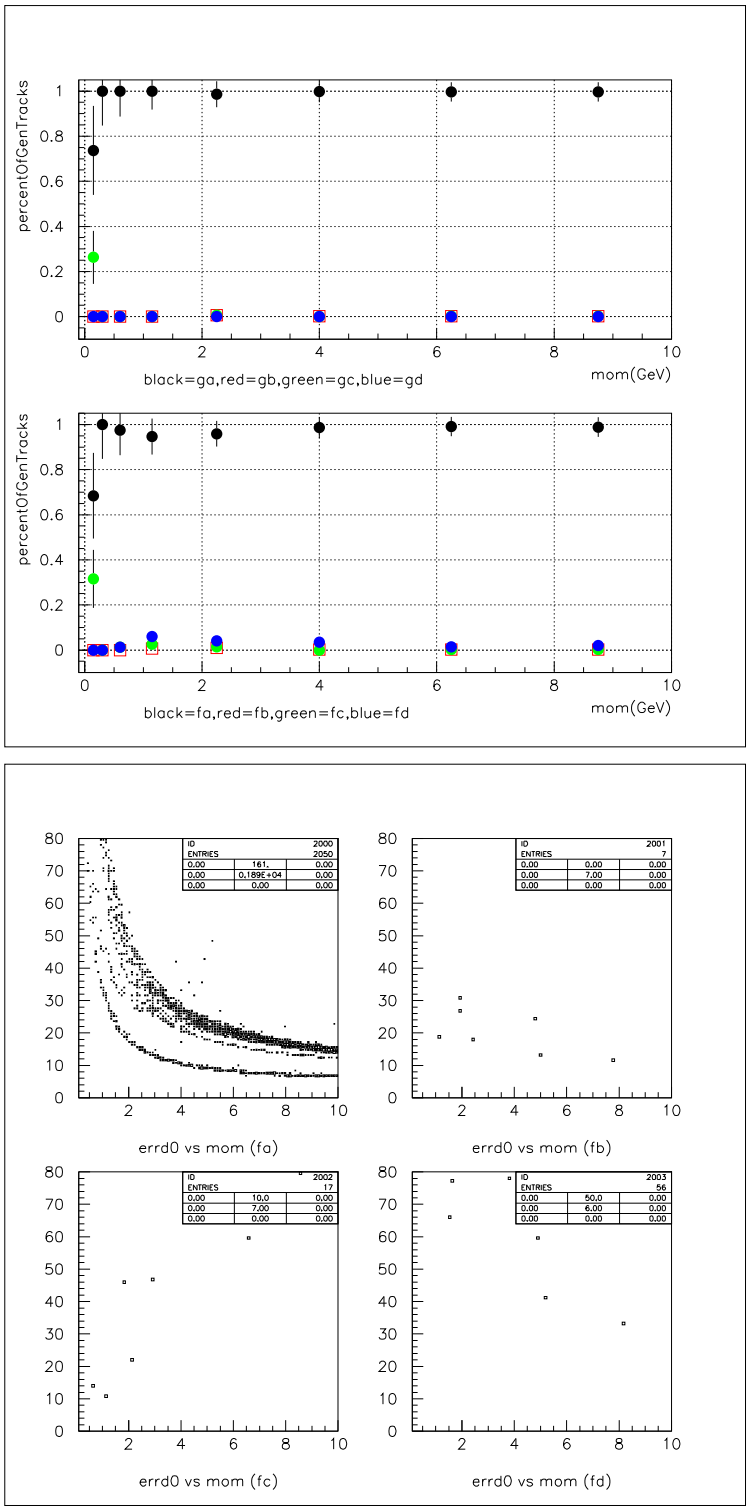

FIGURE 21. G_i and F_i (top) and impact parameter error in $r\phi$ (in μm) versus momentum (in GeV) for the different F_i (bottom), for polar angle range $12 - 17^\circ$ pion tracks.

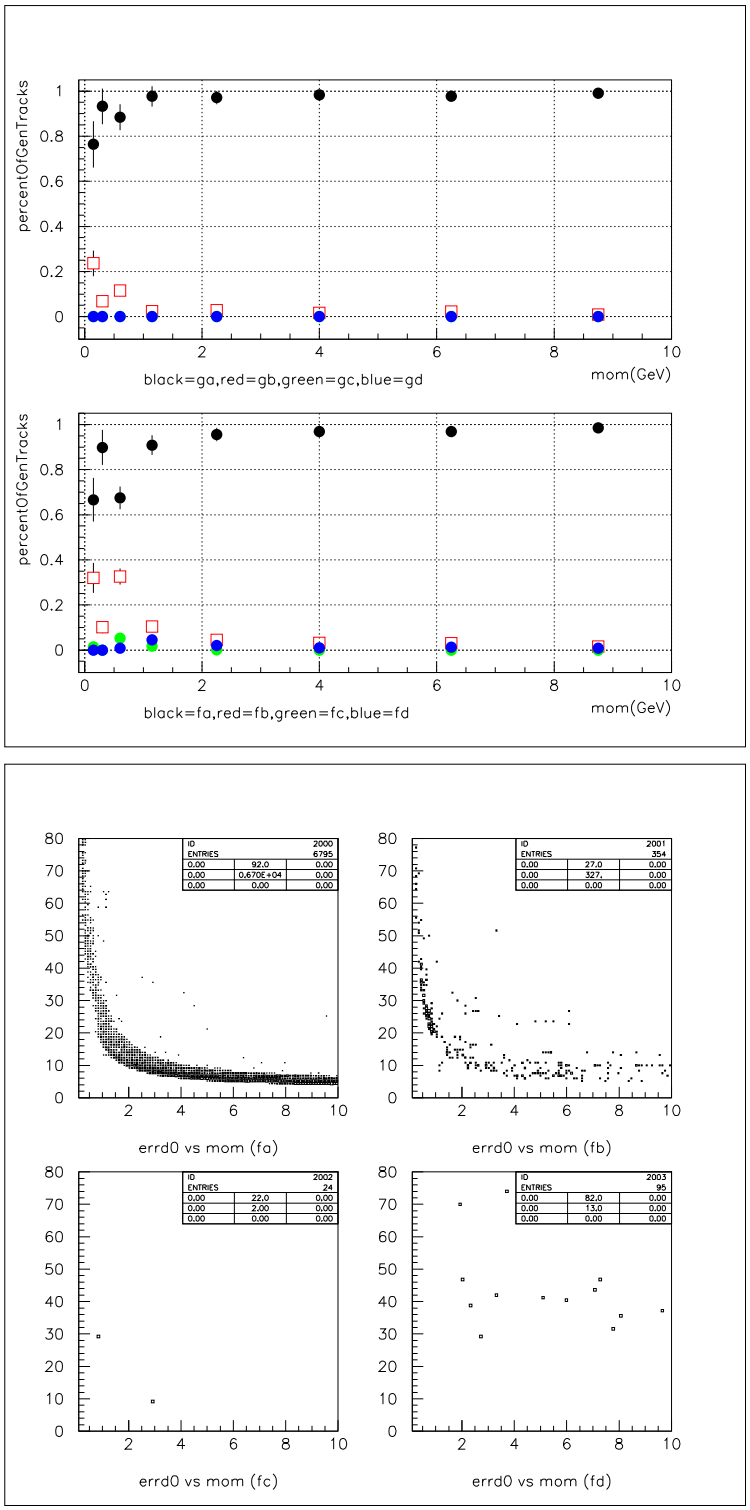

FIGURE 22. G_i and F_i (top) and impact parameter error in $r\phi$ (in μm) versus momentum (in GeV) for the different F_i (bottom), for polar angle range $17 - 30^\circ$ pion tracks.

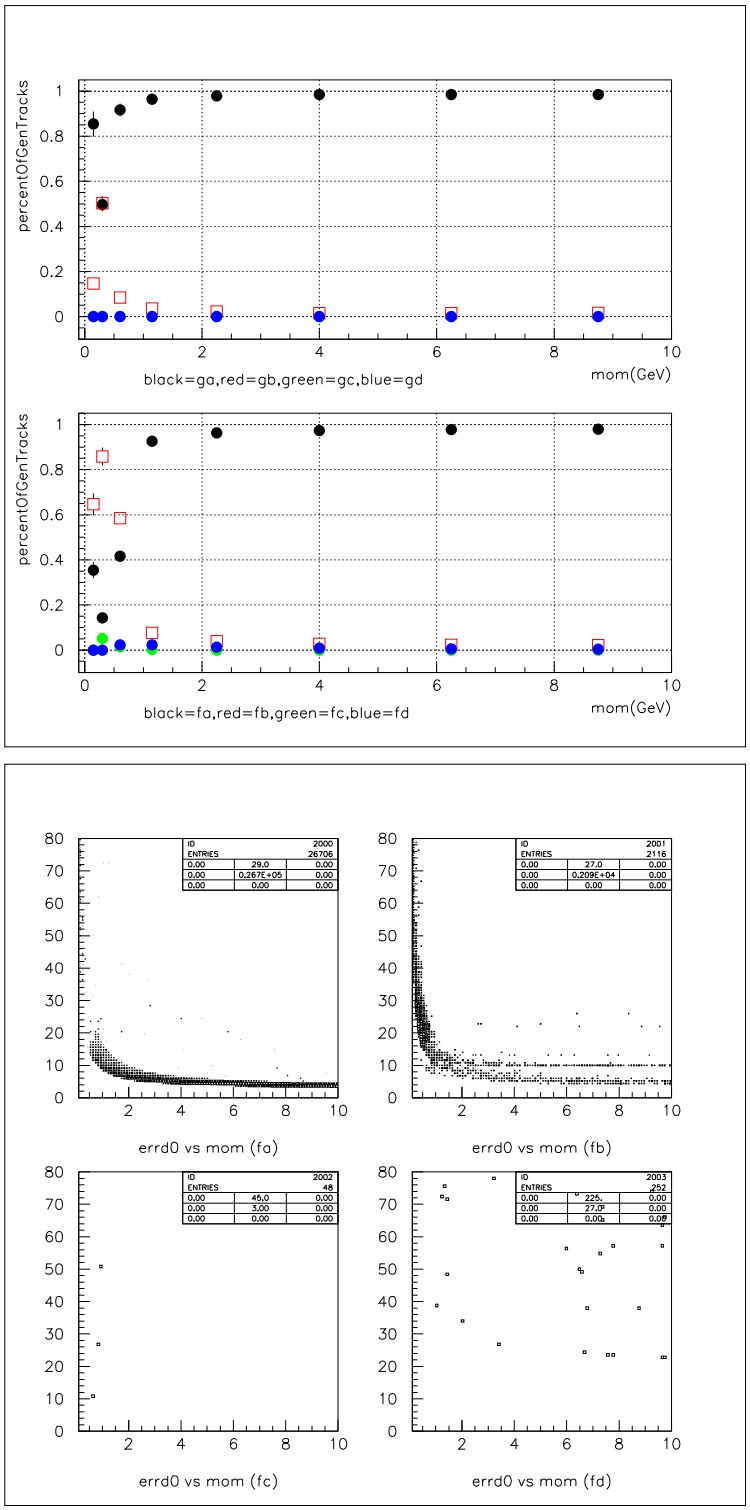

FIGURE 23. G_i and F_i (top) and impact parameter error in $r\phi$ (in μm) versus momentum (in GeV) for the different F_i (bottom), for polar angle range $30 - 60°$ pion tracks.

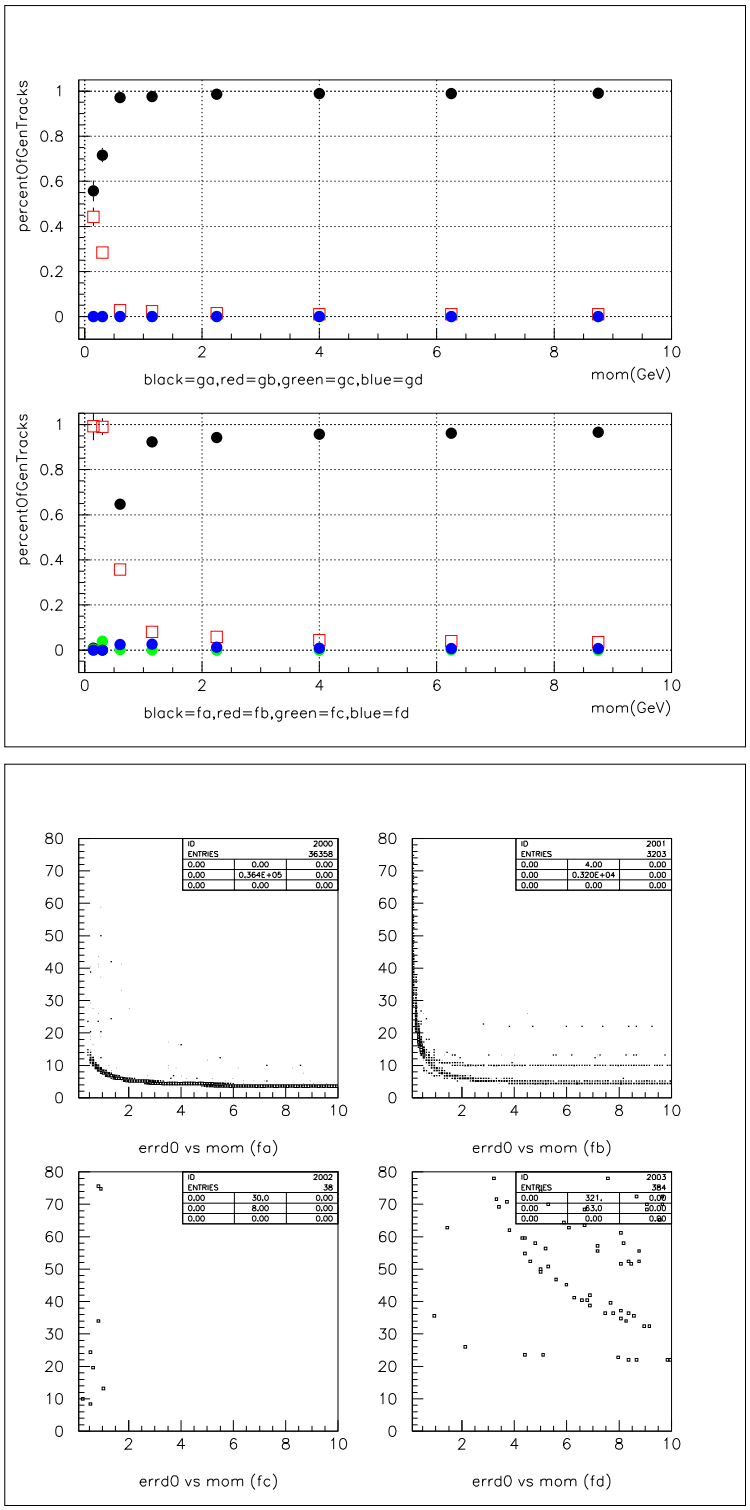

FIGURE 24. G_i and F_i (top) and impact parameter error in $r\phi$ (in μm) versus momentum (in GeV) for the different F_i (bottom), for polar angle range $60 - 90°$ pion tracks.

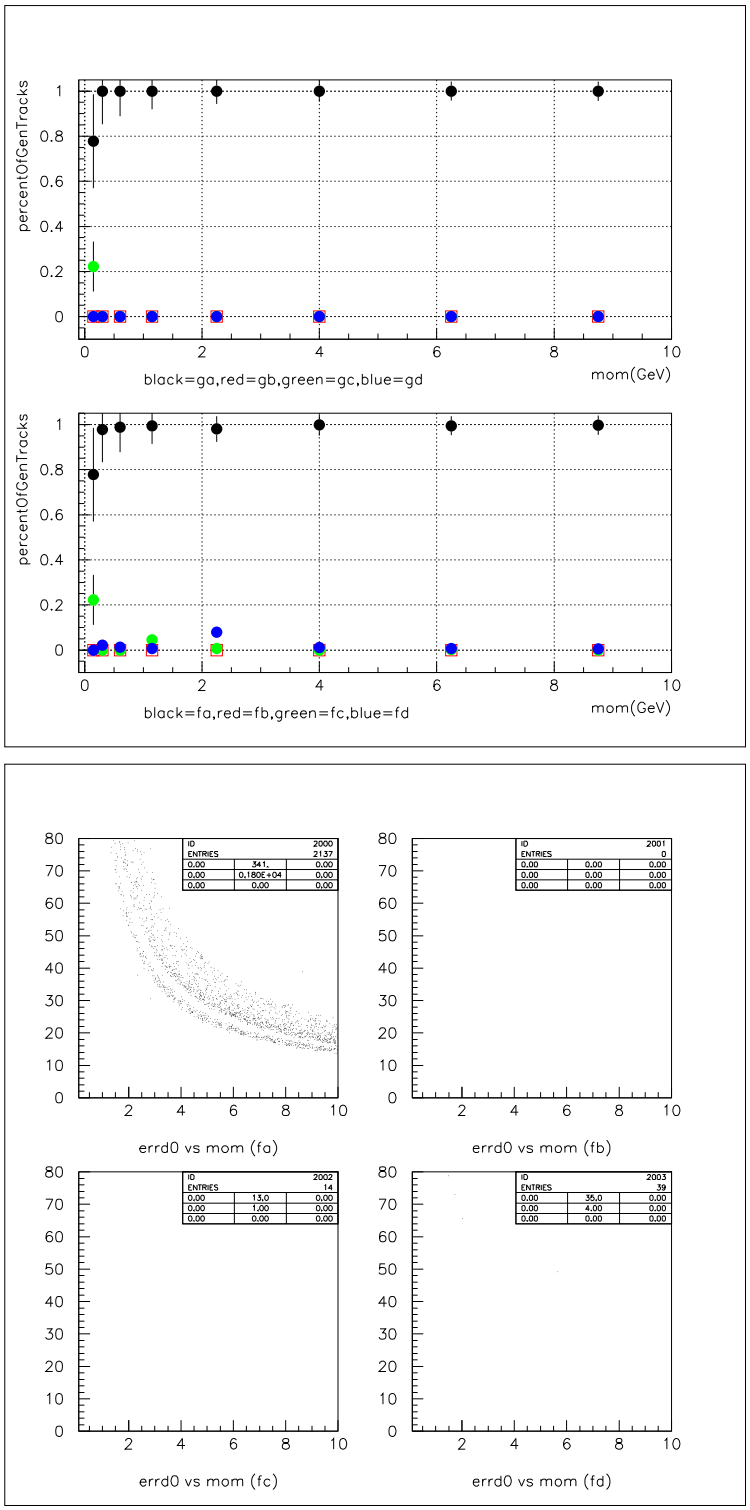

FIGURE 25. G_i and F_i (top) and impact parameter error in $r\phi$ (in μm) versus momentum (in GeV) for the different F_i (bottom), for polar angle range $12 - 17^\circ$ muon tracks.

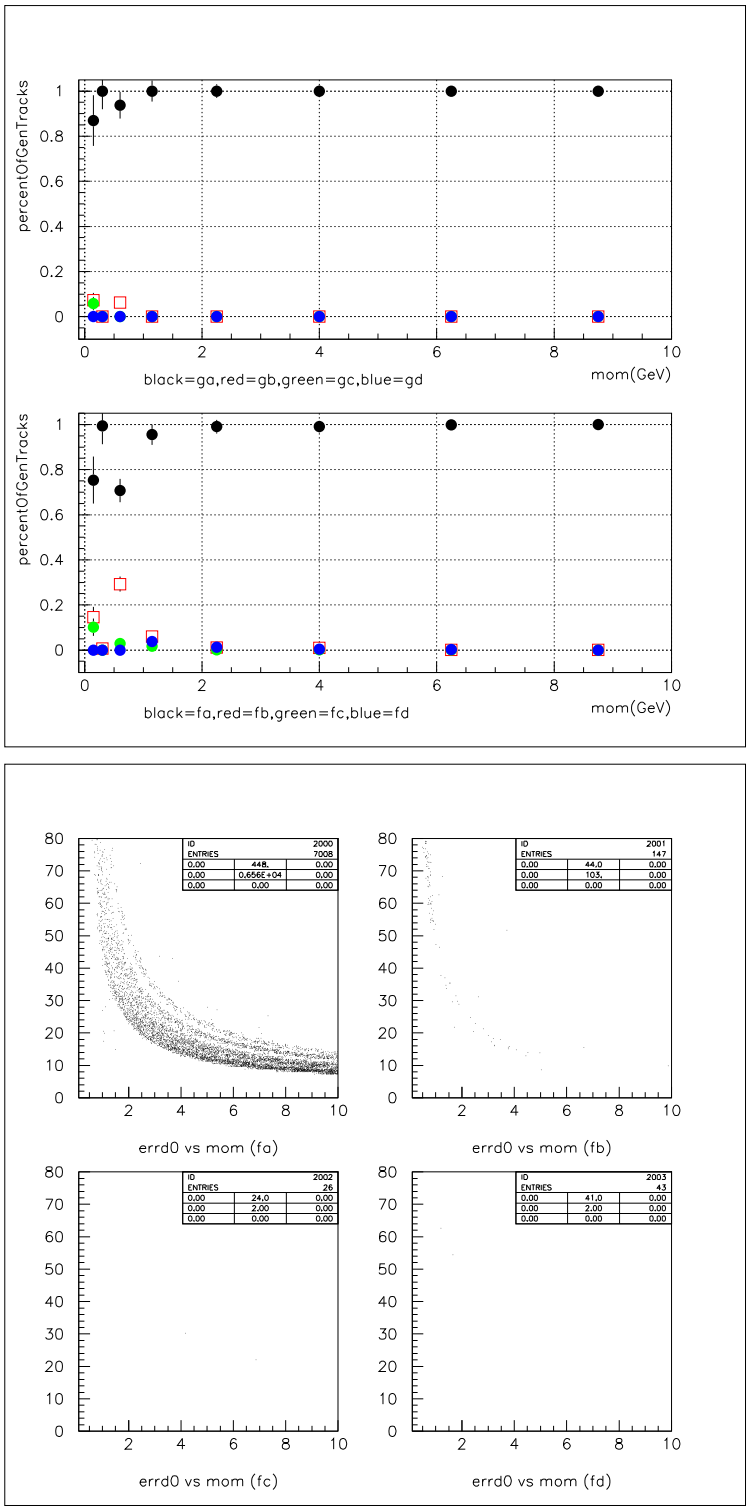

FIGURE 26. G_i and F_i (top) and impact parameter error in $r\phi$ (in μm) versus momentum (in GeV) for the different F_i (bottom), for polar angle range $17 - 30^\circ$ muon tracks.

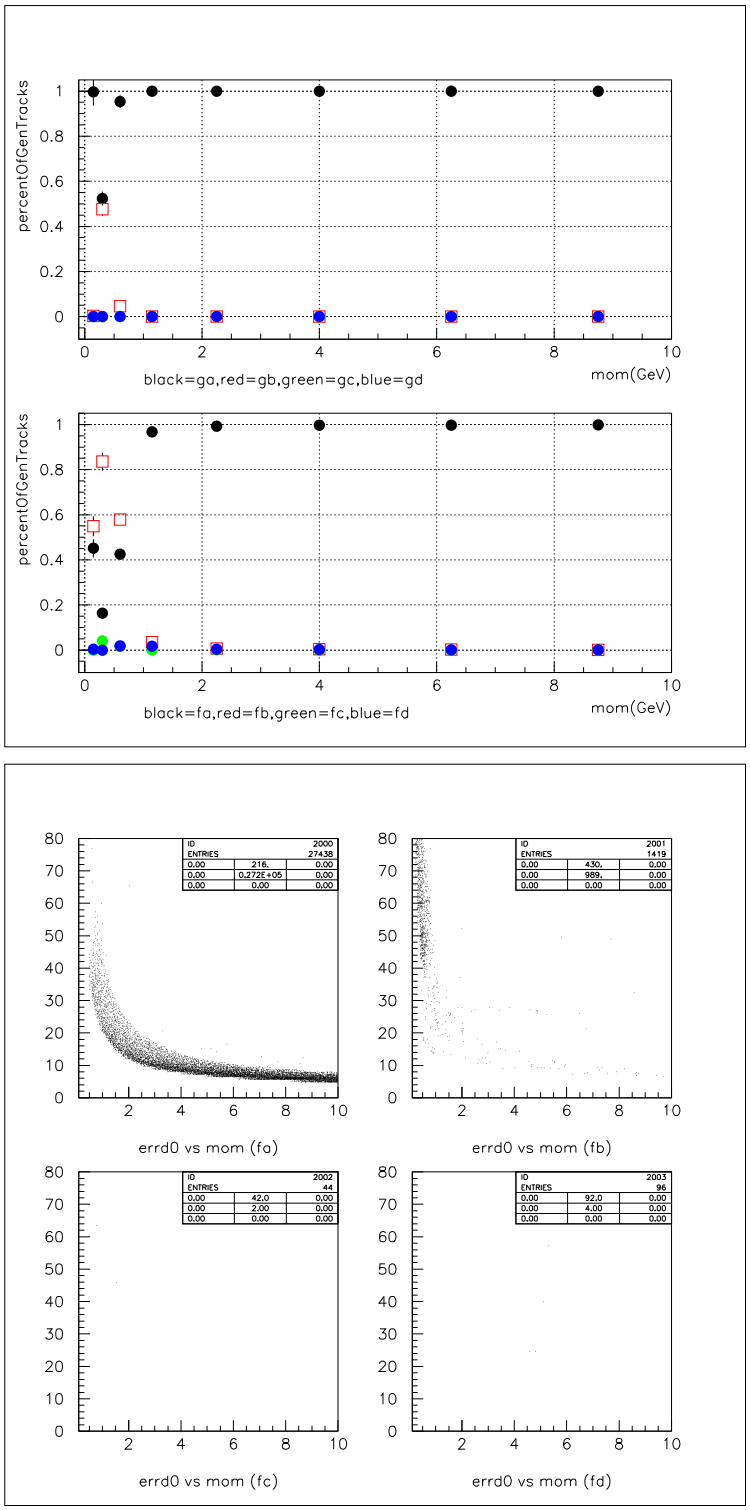

FIGURE 27. G_i and F_i (top) and impact parameter error in $r\phi$ (in μm) versus momentum (in GeV) for the different F_i (bottom), for polar angle range $30 - 60^\circ$ muon tracks.

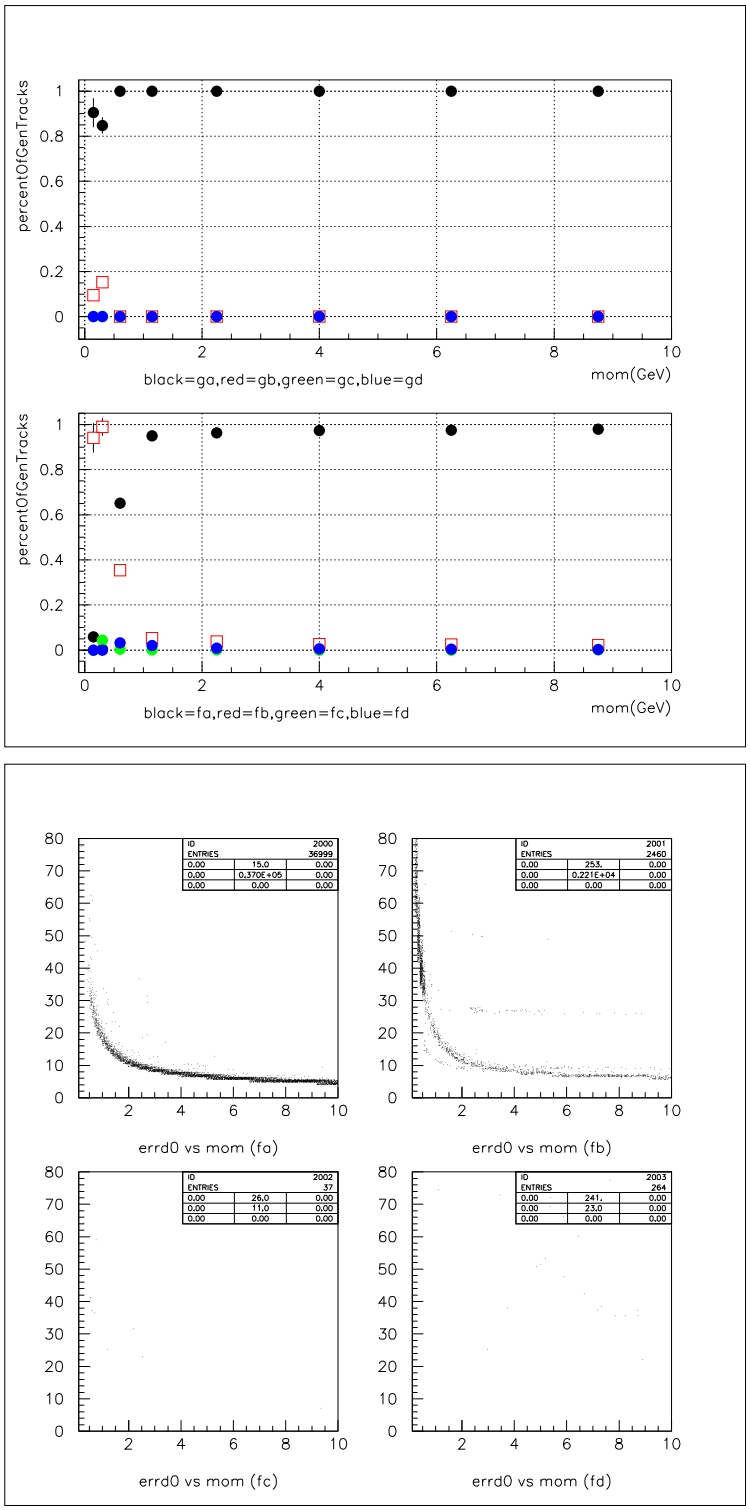

FIGURE 28. G_i and F_i (top) and impact parameter error in $r\phi$ (in μm) versus momentum (in GeV) for the different F_i (bottom), for polar angle range $60 - 90^\circ$ muon tracks.

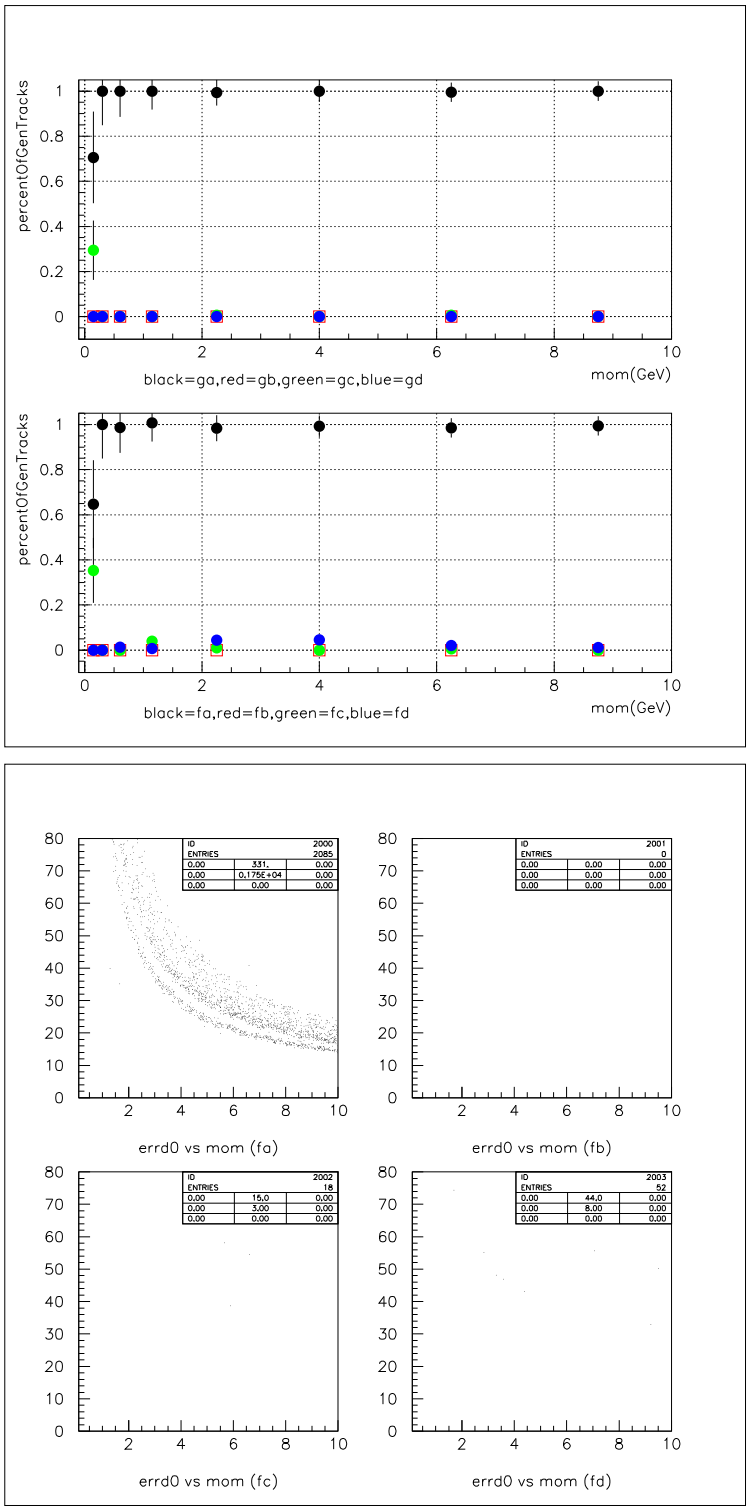

FIGURE 29. G_i and F_i (top) and impact parameter error in $r\phi$ (in μm) versus momentum (in GeV) for the different F_i (bottom), for polar angle range $12 - 17^\circ$ pion tracks.

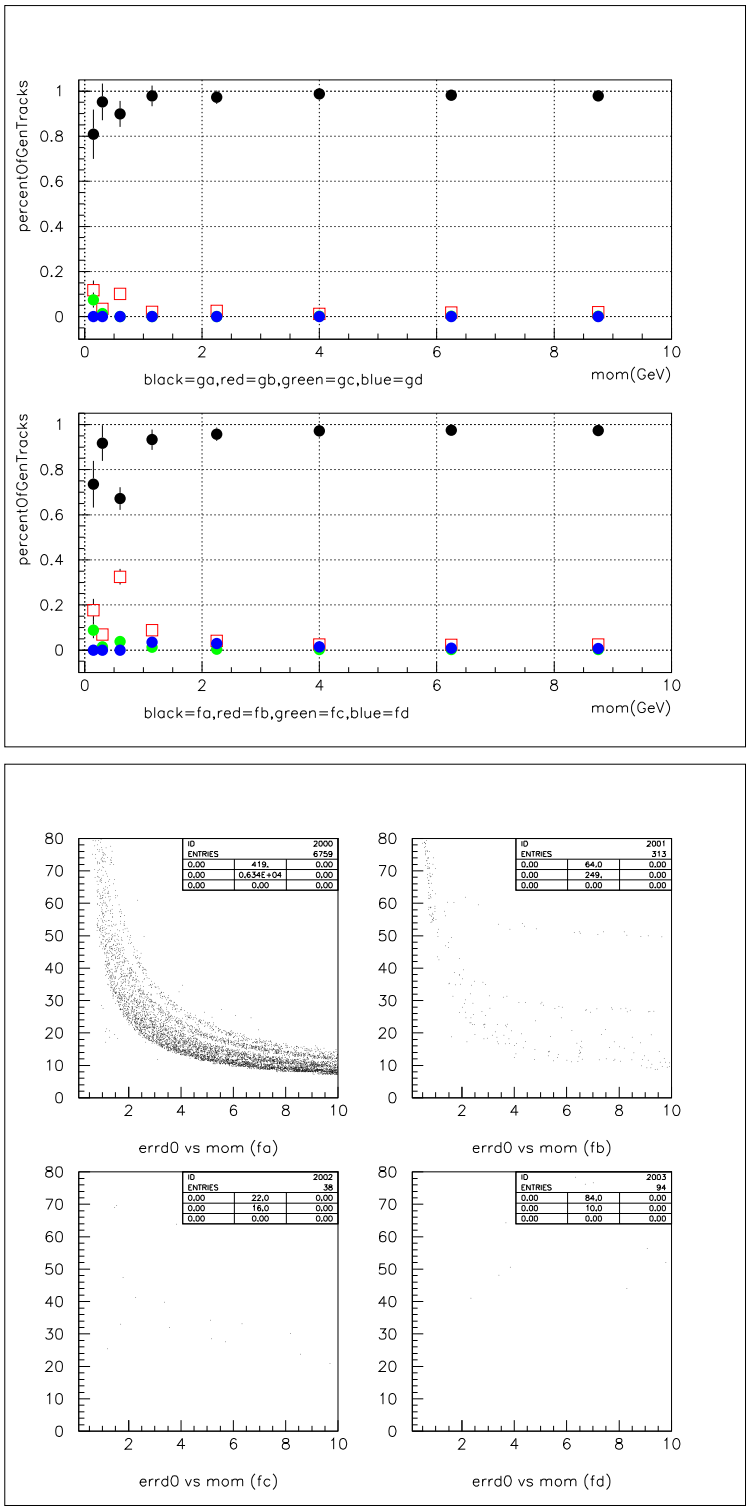

FIGURE 30. G_i and F_i (top) and impact parameter error in $r\phi$ (in μm) versus momentum (in GeV) for the different F_i (bottom), for polar angle range $17 - 30^\circ$ pion tracks.

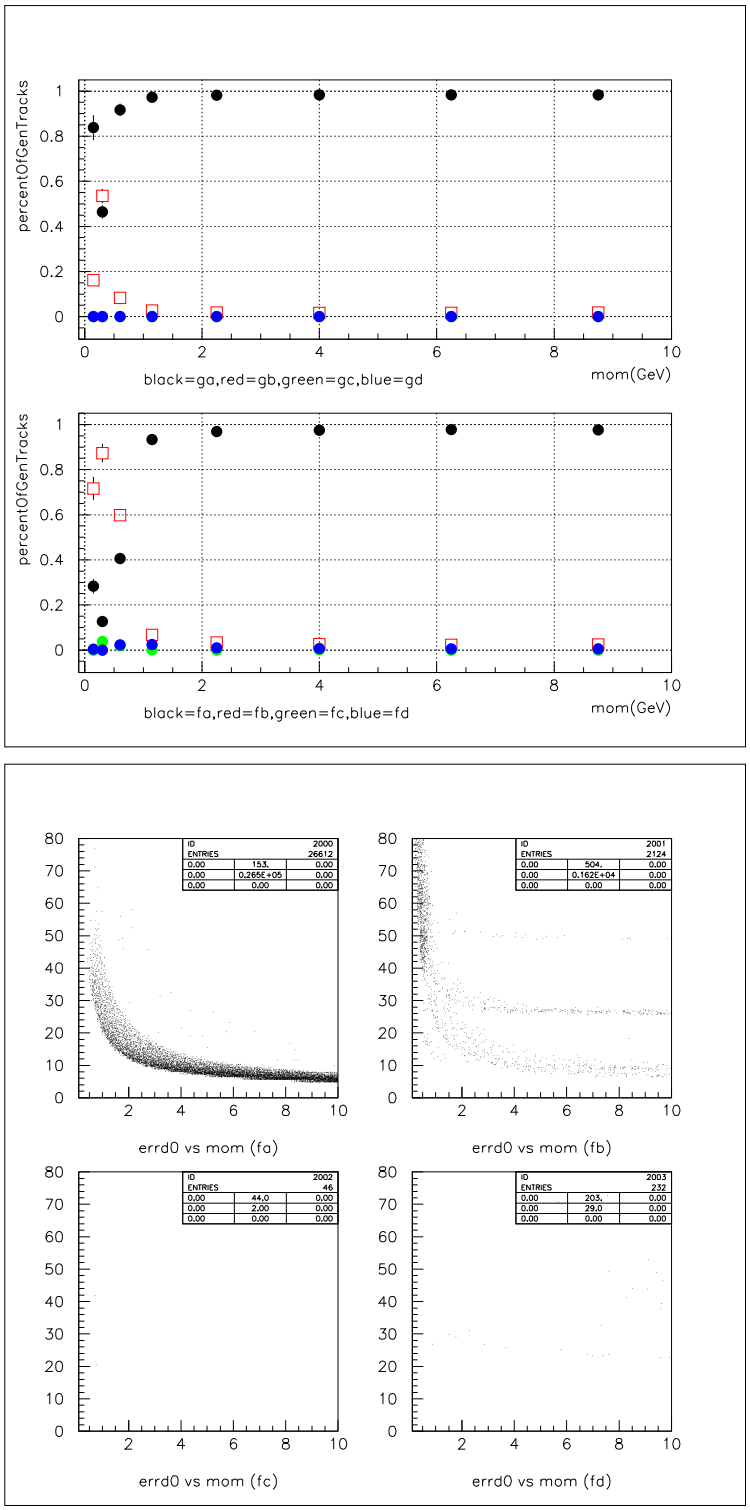

FIGURE 31. G_i and F_i (top) and impact parameter error in $r\phi$ (in μm) versus momentum (in GeV) for the different F_i (bottom), for polar angle range $30 - 60°$ pion tracks.

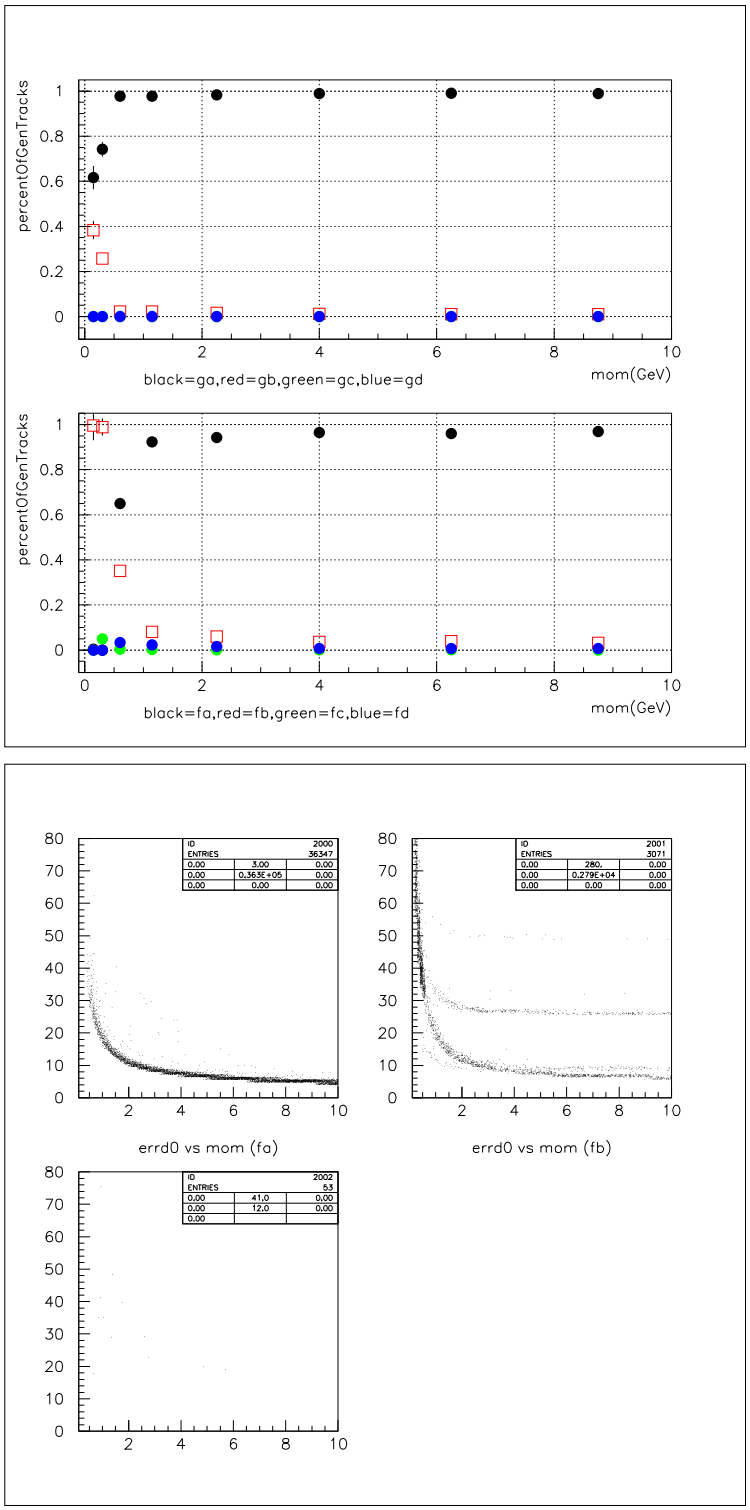

FIGURE 32. G_i and F_i (top) and impact parameter error in $r\phi$ (in μm) versus momentum (in GeV) for the different F_i (bottom), for polar angle range $60 - 90°$ pion tracks.